technische universität
dortmund

fakultät
physik

Diagrammatic approach to thermal fluctuations in dimension 2

Master's thesis by

Jan Denkers

born in Recklinghausen

submitted to Lehrstuhl für Theoretische Physik I
Fakultät Physik
TU Dortmund

supervised by Prof. Dr. Götz Uhrig

second corrector Priv.-Doz. Dr. Ute Löw

March 2017

Abstract

Fauseweh et al. showed that the observed asymmetry of the spectral function in inelastic neutron scattering experiments of some dimer systems can be understood solely by the thermal behavior of free hardcore boson excitation in one dimension. In this thesis we investigate the behavior of the Brückner approach they used in higher dimensions. We will make use of effective models to describe the 2D-crystals VOPO and Cs_2CuCl_4 on the basis of hardcore bosons. In addition, a toy model was used to examine the influence of the dimensionality in a more systematic fashion. We find that the approach leads to similar results in higher dimensions. In particular we confirm that the additional space leads to a decrease in the effects of broadening and asymmetry. On the other hand we also find that the change in particle number and peak position differs from the hypothesized behavior.

Contents

1 Introduction

To describe the dynamics of many-body quantum systems, we need to combine various techniques to break down the problem into solvable parts. Two phenomena in particular lead to complications in practical calculations: Quantum fluctuations and thermal fluctuations. These problems often arise in the context of magnetic models, which are particularly interesting since they can be described with some of the simplest Hilbert-spaces in many-body physics and are experimentally well accessible. Some of these systems can be modeled with effective hardcore bosonic particles. Their quantum fluctuations might be treated with CUTs [1, 2, 3] or variational approaches [4], resulting in particle-conserving Hamiltonians that can be understood as an effective model of ground state, propagation and scattering of the conserved excitations. However, the thermal fluctuations lead to dynamics that cannot yet in general be analytically captured: For the simplest of such cases, the free hardcore bosonic model in 2 or 3 dimensions, most strategies suffer from either being applicable only to small systems, like direct diagonalization [5], or exhibiting non-physical behavior like the $1/z$ expansion by Jensen [6]. A recent perturbative approach by Fauseweh et al. [7, 8] overcomes these issues and provides a description of this model in the low temperature limit and in the presence of a gap in the dispersion relation. This approach has the advantage that it is applicable to arbitrary dimensions. The extension to higher dimensions seems promising, since there is more space to avoid a pile-up of excitations even at higher temperatures, making the hardcore constraint less problematic.

In this thesis we want to describe this approach, present a software framework to find numerical solutions for the propagator and use that to investigate the effect of dimensionality on the behavior of the system. Magnetic systems that are believed to be accurately described by hardcore excitations show asymmetric broadening and band narrowing in their neutron scattering spectrum which we want to understand. Since most substances behave like effective two- or three-dimensional systems, we want to confirm that the findings from one dimension are still valid in higher dimensions.

We start with experimental observations that raised the interest in the description of thermal effects in free hardcore bosonic models. In chapters 3 and 4 we review two substances that can be described as effective 2D hardcore bosonic systems as a motivation for the importance of such models and as the setting for our later calculations. We then describe the perturbative Brückner approach for the calculation of the spectral function of the propagator in chapter 5. In chapter 6 we outline how to perform the calculations on a computing cluster with a framework optimized for performance and memory efficiency. In the following chapter we present our findings in terms of numerical calculations. Finally, we conclude and give an outlook in chapter 8.

2 Experimental Observations on Hardcore Bosonic Systems

In this chapter we give a brief overview of the observations in experiments that motivate the investigation of the properties of hardcore bosonic models with the Brückner Method. In the first section we outline what experimentally observed effects we are focusing on in our numerical study. The second section introduce hardcore bosons as a possible theoretical foundation.

2.1 Anomalies in Scattering Data

While earlier experiments seemed to suggest a universal symmetric Lorentzian curve shape for the propagator's spectral function $A^\alpha(p,\omega)$ in frequency space[9, 10] in all magnetic models, recent studies however find asymmetric curve shapes in some dimerized systems[11]. Besides the asymmetry a narrowing of the band with increasing temperature for the single particle mode was observed as well [12]. Figure 1 shows an example of an observation of asymmetry in $Cu(NO_3)_2 \cdot 2,5D_2O$ crystals and Figure 2 depicts a measurement that has observed the band narrowing effect.

This data is accessible by inelastic neutron scattering. Figure 3 depicts a schematic neutron scattering experiment. Assuming $\hbar\omega = E - E'$ denotes the energy transfer, $\mathbf{Q} = \mathbf{k} - \mathbf{k}'$ the momentum transfer and $S^\alpha(t)$ the spin operator at time t, we define our observable, the dynamic structure factor, as

$$S^{\alpha\beta}(\mathbf{Q},\omega) = \frac{1}{N}\sum_{l,n}\int_{-\infty}^{\infty} dt \exp\left[-i(\mathbf{Q}\cdot\mathbf{R}_n - \omega t)\right]\left\langle S_l^\alpha(t) S_{l+n}^\beta(0)\right\rangle,\ \alpha,\beta\in\{x,y,z\}. \tag{1}$$

It is the time and space Fourier transform of the spin-spin correlation. By the fluctuation-dissipation theorem it is related to the spectral function of the propagator. As an example, a relation for the crystal Cs_2CuCl_4, which we discuss in the next chapter, is given by

$$S^{xx}(\mathbf{Q},\omega) = \frac{1}{4}\frac{1}{1-e^{-\beta\omega}}(A(\mathbf{k},\omega) + A(-\mathbf{k},\omega)). \tag{2}$$

One thing all systems which exhibit effects like the asymmetry of the spectral function have in common is the existance of hardcore bosonic excitations with a gapped band. Therefore we focus on hardcore bosonic models and show that all it takes to describe these effects are free hardcore bosonic systems.

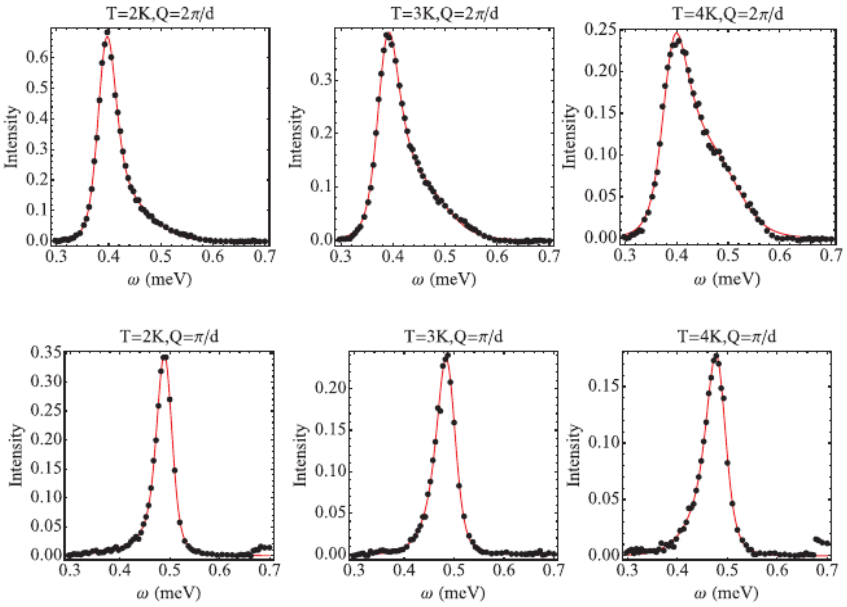

FIG. 1. Inelastic neutron scattering experiment on the $Cu(NO_3)_2 \cdot 2,5D_2O$ crystal. Upper half shows the gap mode and the lower half the maximum mode. Figure taken from Ref.[13].

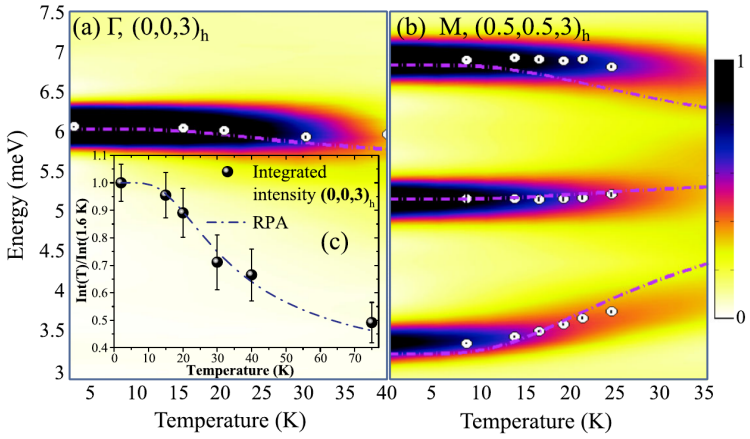

FIG. 2. Spectrum of $Sr_3Cr_2O_8$ in an inelastic neutron scattering experiment. Performed constant-wave-vector scans at a) $(0,0,3)_h$, b) $(0.5,0.5,3)_h$ on FLEX. c) shows a integrated intensity with respect to temperature of the excitation at $(0,0,3)_h$. Dashed lines depict random phase approximations. Figure taken from Ref.[14].

2.2 Hardcore Boson Systems

In quantum magnets, a variety of elementary excitations like spin flips and triplon excitations have at least one thing in common: They obey a local hardcore constraint,

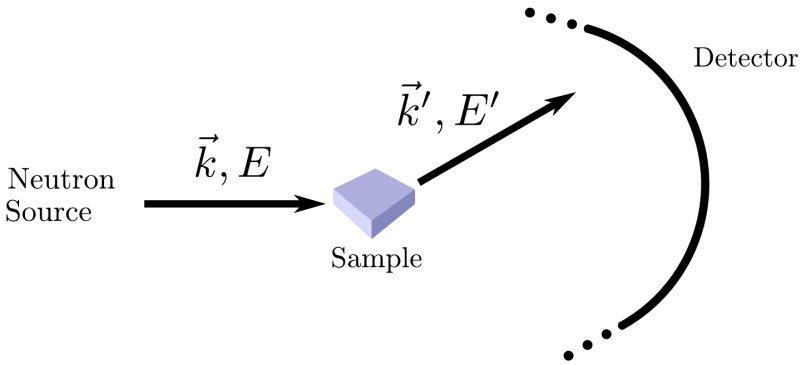

FIG. 3. Schematic experimental inelastic neutron scattering setup. Figure taken from Ref.[15]

exhibiting the peculiar commutation relations

$$[b_{j,\alpha}, b^\dagger_{i,\beta}] = \delta_{i,j}\left(\delta_{\alpha\beta}\left(1 - \sum_\gamma b^\dagger_{i\gamma} b_{i\gamma}\right) - b^\dagger_{i,\beta} b_{i,\alpha}\right), \quad [b_{i,\alpha}, b_{j,\beta}] = 0, \tag{3}$$

where $b^\dagger_{j,\alpha}$ is the creation operator, latin indices specify a lattice position and greek indices label the flavor of the hardcore boson. We use a simple single index notation without a vector arrow to denote positions and momentum in one, two or three dimensions. The commutator behaves like a bosonic commutation relation on different sites, but forbids the occupation of a single site for more than one boson of an arbitrary flavor, just like fermions do. This is a strong restriction for the hilbert space. Surprisingly, this combination of both statistics creates a much more complicated behavior in the free theory. We consider the Hamiltonian

$$H = E_0 + \sum_{i,d,\alpha} w^\alpha_d b^\dagger_{i,\alpha} b_{i+d,\alpha} + \text{H.c.}\,. \tag{4}$$

In contrast to the bosonic or fermionic free theory, this model is neither solved nor well understood. We Fourier-transform

$$b^\dagger_{j,\alpha} = \frac{1}{\sqrt{N}} \sum_q e^{iqj} b^\dagger_{q,\alpha} \tag{5}$$

into momentum space, yielding

$$H = \sum_{q\alpha} \omega^\alpha(q) b^\dagger_{q,\alpha} b_{q,\alpha}. \tag{6}$$

The commutator now takes the form

$$[b_{k,\alpha}, b^\dagger_{k',\beta}] = \frac{1}{L}\sum_q \left(\delta_{\alpha,\beta}\left(1 - \sum_\gamma b^\dagger_{k'+q,\gamma} b_{k+q,\gamma}\right) - b^\dagger_{k'+q,\beta} b_{k+q,\alpha}\right). \tag{7}$$

For the description of the propagator we introduce the Greens-function

$$G^\alpha(j,\tau) = -\langle T b^\dagger_{j,\alpha}(-i\tau) b_{0,\alpha}(0)\rangle \quad \tau \in \mathbb{R}. \tag{8}$$

Here, τ represents the imaginary time, the T is the time ordering superoperator and $b^\dagger_{j,\alpha}(t)$ is the creation operator at time t and site j on a lattice of the quasi-particle of type α. We denote the momentum space Matsubara representation of the Greens-function as $G^\alpha(p,\omega)$ and introduce the spectral function $A^\alpha(p,x)$ via

$$G^\alpha(p,\omega) =: \int_{-\infty}^{\infty} \frac{A^\alpha(p,x)}{\omega - x} dx. \tag{9}$$

If a single quasi-particle is isolated by a gap and if the Hamiltonian is block-diagonal in the one-particle subspace, then the particle can propagate freely, yielding a spectral function

$$A^\alpha(p,\omega) = \delta(\omega - \omega^\alpha(p)). \tag{10}$$

For bosons and fermions, the sum-rule is a constant with respect to temperature. Since the commutator of hardcore bosons is not a scalar we instead obtain a temperature-dependent sum rule given by

$$\int_{-\infty}^{\infty} A(x,k)dx = \left\langle [b_{k,\alpha}, b^\dagger_{k,\alpha}] \right\rangle = 1 - (1+N_f)n(T), \tag{11}$$

where N_f should be interpreted as the number of different flavors and define $n(T) := \frac{1}{N}\sum_k < b^\dagger_k b_k >$. This equation requires that the Hamiltonian is degenerate with respect to the flavor. For zero temperature the thermal occupation vanishes, since our vacuum is particle-free, and we retrieve the bosonic sum rule. In the high temperature limit, each state has the same probability to be occupied and therefore $n(T) = \frac{1}{1+N_f}$ holds. For temperatures in between, there exist no exact known solution in every dimension to our knowledge. In the one-dimensional case with next neighbor hopping $n(T)$ is given by the Fermi-function [8].

3 Review of the Effective Theory of Cs_2CuCl_4

This chapter will describe properties of Cs_2CuCl_4 and their description in a hardcore bosonic model. We will start by presenting the crystal structure of Cs_2CuCl_4 and proceed to outline the most important interaction paths. An effective model containing these interactions in the presence of an external magnetic field will then be transformed into a hardcore bosonic model and a mean-field approximation will be applied for the residual interaction to end up with a non-interacting hardcore bosonic model. This will allow us to use the techniques of chapter 5 to calculate the spectral function of the propagator. Finally we provide a sampling mesh of the Brillouin zone needed for numerical calculations.

3.1 Crystal Structure

Cs_2CuCl_4 is an antiferromagnetic Mott insulator with an orthorhombic crystal structure (Pnma). Its structure is depicted in Figure 4. At $T = 0.3$ K its lattice parameters are given by $a = 9.65$ $\mathring{A}$, $b = 7.48$ $\mathring{A}$, and $c = 12.26$ $\mathring{A}$ [16]. The bc-plane is spanned by $CuCl_4^{2-}$-tetrahedra separated by by Cs^{2+} ions in a-direction. The crystal has been studied for various effects such as spin-liquid behavior[17], dynamic structure factor[18], Bose-Einstein condensation of magnons[19], electron spin resonance spectra[20] and more.

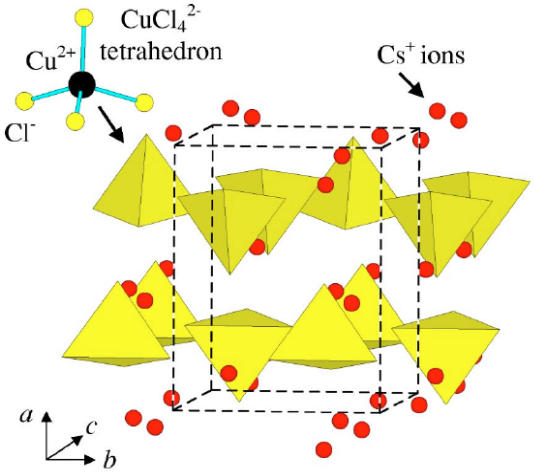

FIG. 4. The crystal structure of Cs_2CuCl_4. Figure is taken from Ref. [16]

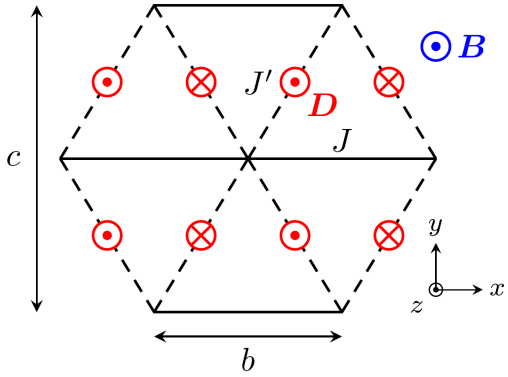

FIG. 5. Reduced lattice model of Cs_2CuCl_4 with respect to the spins of the Cs^{2+} ions. Solid lines denote the strongest exchange path with coupling J. Dashed lines represent the next strongest diagonal nearest-neighbor interaction J'. Red circles mark the Dzyaloshinskii-Moriya interactions along the diagonal in direction $\hat{z}$, where a dot represent a positive and a cross a negative orientation. A magnetic field B points along the $\hat{z}$-direction. Figure is taken from Ref. [21]

3.2 Spin Hamilton Operator

The Spin Hamiltonian we derive will describe the interaction of the Cu^{2+} ions, which each carry a spin of 1/2. The superexchange paths are mediated by the Cl^- ions. Since this path is non-magnetic it lies extremely low in energy at 1–4 K[16]. It is therefore appropriate to describe this substance as an effective 2D-model. The strongest path, which we denote with its coupling strength J, connects nearest-neighbor spins along the $b-$axis and the next strongest path with coupling J' connects spin along the diagonals. Small spin-orbit couplings lead to Dzyaloshinskii-Moriya interactions $\boldsymbol{D} = \pm D\hat{z}$ which also connected neighboring spins along the diagonals. Depending on the diagonal path it has different orientations, see figure 5. In addition we assume an external magnetic field B along the $\hat{z}$ direction. This will lead to a gap in the dispersion relation, which is necessary for the techniques in chapter 5. Coldea, Tennant et al.[19] find for the coupling constants $J = 0.374(5)$ meV$= 4.34(6)$ K, $J'/J = 0.34(3)$ and $D/J = 0.053(5)$. The neglected weak interlayer coupling has a value of $J''/J = 0.045(5)$[19].

The full Hamiltonian reads

$$H = \frac{1}{2}\sum_{i,j}[J_{i,j}\boldsymbol{S}_i\boldsymbol{S}_j + D_{i,j}\cdot(\boldsymbol{S}_i \times \boldsymbol{S_j})] - h\sum_i S_i^z, \tag{12}$$

where $\boldsymbol{R}_i$ is the vector to lattice site i so that $\boldsymbol{S}_i = \boldsymbol{S}(\boldsymbol{R}_i)$ is the spin-1/2 operator at site i. The exchange couplings $J_{i,j} = J(\boldsymbol{R}_i - \boldsymbol{R}_j)$ and $\mathbf{D}_{i,j} = D(\boldsymbol{R}_i - \boldsymbol{R}_j)\hat{z}$ should be understood in the same manner. The first term of the Hamiltonian represents the exchange interaction, the second the Dzyaloshinskii-Moriya interactions and the last the coupling to the external magnetic field h. The effective g-factor of the substance is $g = 2.19(1)$ [21].

Their couplings depend on the connection path $\boldsymbol{R}_i - \boldsymbol{R}_j$. We introduce the symbol δ_k, $k \in \{1, 2, 3\}$ for the three possible paths as

$$\delta_1 = b\hat{x}, \quad \delta_2 = -\frac{b}{2}\hat{x} + \frac{c}{2}\hat{y}, \quad \delta_3 = -\frac{b}{2}\hat{x} - \frac{c}{2}\hat{y}, \tag{13}$$

where $\hat{x}$, $\hat{y}$, $\hat{z}$ are the unit vectors of the regular Cartesian coordinate system. With respect to this symbol the paths have the following coupling constants: $J(\pm\delta_1) = J$, $J(\pm\delta_2) = J(\pm\delta_3) = J'$ and $D(\pm\delta_2) = D(\pm\delta_3) = \mp D$.

3.3 Effective Hardcore Boson Description

Starting from the Hamiltonian (12) in terms of spin ladder operators we will now switch to a hardcore bosonic representation. We relate the ladder operators to the hardcore bosonic creation and annihilation operators through

$$S_i^+ = b_i, \quad S_i^- = b_i^\dagger, \quad S_i^z = 1/2 - b_i^\dagger b_i, \tag{14}$$

so that an excited hardcore boson corresponds to a magnon excitation of the spin system. We treat hardcore bosonic operators as regular bosonic operators with infinite on-site repulsion, which was shown to be possible in [7] . In the rest of this chapter we implicitly assume the existence of such an interaction term. The exact procedure is outlined in chapter 5. The Fourier-transformed coupling constants, which we need in the momentum space representation of the Hamiltonian, are defined via

$$J_{\mathbf{k}} = \sum_R J(\mathbf{R}) e^{-i\mathbf{k}\cdot\mathbf{R}} = 2J\cos(k_x b) + 4J'\cos\left(\frac{k_x b}{2}\right)\cos\left(\frac{k_y c}{2}\right) \tag{15}$$

$$D_{\mathbf{k}} = \sum_{\mathbf{R}} D(\mathbf{R}) e^{-i\mathbf{k}\cdot\mathbf{R}} = -4iD\cos\left(\frac{k_x b}{2}\right)\cos\left(\frac{k_y c}{2}\right), \tag{16}$$

Using the momentum space representation $b_{\mathbf{k}}^\dagger = \frac{1}{\sqrt{N}}\sum_i e^{i\mathbf{k}\mathbf{R}_i} b_i^\dagger$ of the bosonic operators we bring the Hamiltonian into the form

$$H = \sum_{\mathbf{k}} \omega(\mathbf{k}) b_{\mathbf{k}}^\dagger b_{\mathbf{k}} + \frac{1}{2N}\sum_{\mathbf{k},\mathbf{k}',\mathbf{q}} J_{\mathbf{q}} b_{\mathbf{k}+\mathbf{q}}^\dagger b_{\mathbf{k}'-\mathbf{q}}^\dagger b_{\mathbf{k}'} b_{\mathbf{k}} + E_0, \tag{17}$$

where we introduced the dispersion relation

$$\omega(\mathbf{k}) = \frac{1}{2}(J_{\mathbf{k}} - iD_{\mathbf{k}} - J_{\mathbf{0}} + iD_{\mathbf{0}}) + h \tag{18}$$

and energy offset

$$E_0 = N\left(\frac{J_{\mathbf{0}}}{8} - \frac{h}{2}\right). \tag{19}$$

The vacuum of no excited hardcore bosons, which is equivalent to a fully polarized spin system, is only the ground state for a sufficiently strong magnetic field of at least 8.4 T. A magnetic field of $B = 9$ T leads to a vacuum state with a gap Δ of approximately 19% of the coupling J.

3.4 Mean-Field Decoupling

Since the diagrammatic approach in chapter 5 is designed to treat free models, we need to decouple the interaction terms of the Hamiltonian (17) given by

$$H_{\text{int}} = \frac{1}{2N}\sum_{\mathbf{k},\mathbf{k}',\mathbf{q}} J_{\mathbf{q}} b_{\mathbf{k}+\mathbf{q}}^\dagger b_{\mathbf{k}'-\mathbf{q}}^\dagger b_{\mathbf{k}'} b_{\mathbf{k}} = \frac{1}{2}\sum_{i,j} J_{i,j} b_i^\dagger b_i b_j^\dagger b_j. \tag{20}$$

We start by applying Hartree-Fock decoupling to its real space representation

$$H_{\text{int}} = \frac{1}{2}\sum_{i,j} J_{i,j} b_i^\dagger b_i b_j^\dagger b_j. \tag{21}$$

In the bosonic case this takes the form

$$b_i^\dagger b_i b_j^\dagger b_j \approx n b_j^\dagger b_j + b_i^\dagger b_i n - n^2 + \tau_{j,i} b_i^\dagger b_j + \tau_{i,j} b_j^\dagger b_i - \tau_{ij}\tau_{ji}, \tag{22}$$

where we used

$$n = \left\langle b_i^\dagger b_i \right\rangle, \quad \tau_{i,j} = \left\langle b_i^\dagger b_j \right\rangle. \tag{23}$$

n is independent of i because of the translation invariance of the system. Inserting this approximation into the Hamiltonian H_{int} yields

$$\frac{1}{2}\sum_{i,j} J_{i,j} b_i^\dagger b_i b_j^\dagger b_j \approx \sum_{i,j} J_{i,j}(n b_i^\dagger b_i + \tau_{j,i} b_i^\dagger b_j) + E_{\text{MF}}, \tag{24}$$

where the last term E_{MF} is the constant mean-field contribution given by

$$E_{\text{MF}} = -\frac{1}{2}\sum_{i,j} J_{i,j}(n^2 + \tau_{i,j}\tau_{j,i}), \tag{25}$$

which will be neglected since it is constant. For brevity, we define the constants τ_i, $i \in \{1,2,3\}$ as

$$\tau_1 = \tau(\delta_1), \quad \tau_2 = \tau(\delta_2), \quad \tau_3 = \tau(\delta_3). \tag{26}$$

The reflection invariance of $k_y \to -k_y$ of the Hamiltonian implies $\tau_2 = \tau_3$. Returning to the momentum representation we obtain

$$\frac{1}{2N}\sum_{\mathbf{k},\mathbf{k}',\mathbf{q}} J_{\mathbf{q}} b_{\mathbf{k}+\mathbf{q}}^\dagger b_{\mathbf{k}'-\mathbf{q}}^\dagger b_{\mathbf{k}'} b_{\mathbf{k}} \approx \sum_{\mathbf{k}} (J_{\mathbf{k}}^\tau + n J_0) b_{\mathbf{k}}^\dagger b_{\mathbf{k}}, \tag{27}$$

where

$$J_{\mathbf{k}}^\tau = 2J\text{Re}(\tau_1 e^{i\mathbf{k}\delta_1}) + 2J'\text{Re}(\tau_2 e^{i\mathbf{k}\delta_2} + \tau_3 e^{i\mathbf{k}\delta_3}). \tag{28}$$

The constants could be calculated from momentum space quantities as

$$\tau_i = \tau(\delta_i) = \frac{1}{N}\sum_{\mathbf{k}} n_{\mathbf{k}} e^{-i\mathbf{k}\delta_i} \tag{29}$$

$$n = \frac{1}{N}\sum_{\mathbf{k}} n_{\mathbf{k}} \tag{30}$$

$$n_{\mathbf{k}} = \left\langle b_{\mathbf{k}}^\dagger b_{\mathbf{k}} \right\rangle. \tag{31}$$

We conclude that the mean-field decoupling leads to a renormalization of the dispersion relation as

$$\hat{\omega}(\mathbf{k}) = \frac{1}{2}(J_{\mathbf{k}} - iD_{\mathbf{k}} - J_{\mathbf{0}} + iD_{\mathbf{0}}) + h + J_{\mathbf{k}}^\tau + nJ_0. \tag{32}$$

We will apply a selfconsistent treatment to this equation, which we will discuss in section 6.5. We could now consider adding the the on-site repulsion term to enforce the hardcore constraint or consider the operators of the Hamiltonian as hardcore bosonic again. This will be the starting point for the further treatment in chapter 5.

3.5 Discretization of the Brillouin Zone

Since the later treatment of the Hamiltonian requires numerical calculations using Fourier transforms we need to sample the Brillouin zone with respect to an appropriate basis. The requirements that this basis needs to fulfill are described in section 6.1. If the basis of the lattice vectors is given as

$$\mathbf{a}_1 = b\hat{x}, \quad \mathbf{a}_2 = -\frac{b}{2}\hat{x} + \frac{c}{2}\hat{y}, \tag{33}$$

we obtain for the reciprocal basis the vectors

$$\mathbf{b}_1 = \frac{2\pi}{b}\hat{x} + \frac{2\pi}{c}\hat{y}, \quad \mathbf{b}_2 = \frac{4\pi}{c}\hat{y}. \tag{34}$$

With respect to this basis each point of the sampling mesh is given by

$$\mathbf{k} = k_1\mathbf{b}_1 + k_2\mathbf{b}_2. \tag{35}$$

To achieve an uniform sampling of the Brillouin zone the coefficients can take the values

$$k_1 = \frac{l_1}{N}, \quad l_1 \in \{0, \ldots, N-1\} \tag{36}$$

$$k_2 = \frac{l_2}{N}, \quad l_2 \in \{0, \ldots, 2N-1\}, \tag{37}$$

where the parameter $N \in \mathbb{N}$ controls the overall sampling rate.

4 Review of the Effective Theory of $(VO)_2P_2O_7$

In this chapter we will discuss properties of the Vanadyl pyrophosphate crystal (VOPO) and derive a free effective hardcore bosonic model to describe its physics. The hardcore bosonic picture will be the starting point for the calculation of the propagator in chapter 5.

We will first give a brief description of the crystal structure and relevant interaction paths. Starting from a first model of the relevant interactions we turn over to a description in terms of effective magnetic excitations as hardcore bosonic triplons. To obtain a simpler Hamiltonian, we then introduce and apply the Continuous Unitary Transformation (CUT) technique, which allows us to then derive the dispersion relation. Finally, we reference a fit of model parameters.

4.1 Crystal Structure

The crystal structure of VOPO is depicted in Figure 6. The quantum magnets that will be described in this system are the V^{4+} ions with S=1/2. They exhibit a singlet ground state with a spin gap $\Delta = 3.1$ meV[23].

The ions interact via an antiferromagnetic Heisenberg superexchange interaction. Measurements of the structurally related material $VODPO_4 \bullet 1/2D_2O$ revealed which interaction paths are the most important: The strongest interaction path, to which we will assign the coupling strength J_1, is given by the double V-O-P-O-V link along $\hat{b}$. The second-strongest interaction path with coupling J_2 proceeds along the edge-sharing VO_5 square pyramids in direction $\hat{b}$. The ratio of their interaction strengths is given by $\gamma = J_2/J_1 \approx 0.8$. An additional exchange path along V-O-V in direction $\hat{a}$ is negligible. Measurements by inelastic neutron scattering [24] revealed a weak $\hat{c}$ axis coupling, leading to separated planes in the $\hat{a}, \hat{b}$ direction.

Even though there is no obvious reason to expect different behavior among the V^{4+} ions and PO_4 groups in each plane there certainly are two species of planes. This was revealed by NMR measurements of the Knight Shift and relaxation rate $1/T_1$ [25]. The results for the hypothesis of different species of ions however is not completely consistent but still it is clearly related to a different magnetic environment.

The strongest relative deviations in atom spacing between the two types of planes is the interatomic distance in the P-V spacing of order $\mathcal{O}(10^{-2})$ and the deviation in the distance of the V-V spacing of order $\mathcal{O}(10^{-3})$. Although these are relatively small, ab initio calculations of the superexchange interaction show a strong dependence on the interatomic positions and angles [26]. However, a quantitative description with these calculations is still out of reach. Inside each plane two models have been proposed, one is a spin-ladder and the other an alternating chain model. VOPO was long believed

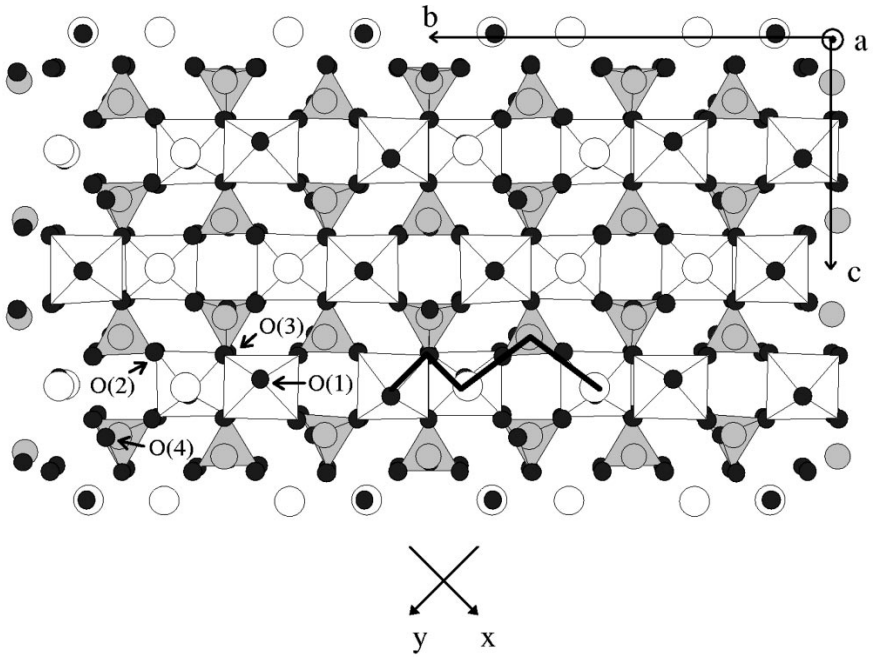

FIG. 6. The crystal structure of VOPO. Vanadium, phosphorus and oxygen atoms are depicted as a white, gray and black circles, respectively. The planes along the b,c direction are stacked in direction a. The VO_6 octahedra form two separated ladders. The P_2O_7 double tetrahedra connect these. The axes b and c are rotated by 45°with respect to x and y. The black line represents a superexchange path. Figure is taken from Ref. [22].

to be the first known crystal that resembles a spin ladder, but newer results from inelastic neutron scattering showed a second low-lying excitation with a gap energy of 5.7 meV which the spin ladder model cannot account for[27]. The alternating chain model on the other hand provides an explanation for this effect as an dimerization.

For this reason we adapt the alternating chain model. They have the couplings $(J_1, J_2)_{A,B}$ and gaps $\Delta_{0,A}$ and $\Delta_{0,B}$, where the indices A, B label different planes.

The chains correspond to eight distinct V atoms per cell grouped into two chains with two dimers each. The reported gap energies $\Delta_{0,A} = 68\text{K}$ and $\Delta_{0,B} = 35\text{K}$ are consistent with the interpretation of two different dispersion curves of magnetic excitations on each plane [25].

4.2 Effective Spin Hamilton Operator

We will now describe an effective Hamiltonian to model the behavior of the system using a minimal set of strongly coupled paths that fit the experimental observations. A complete description of the superexchange paths is still not possible due to a lack of knowledge and computational power[26]. The couplings of the obtained effective Hamiltonian can then be fitted to the experimental data. The most important couplings are related to the $d_{x,y}$ orbitals of the V ions, namely J_1 and J_2, which will therefore be part of the model. The first coupling we discard is the V-O-V path along $\hat{a}$ since it is orthogonal to $d_{x,y}$. Despite their length, two of the V-O-P-O-P-O-V paths are significant since they form an almost 180°angle with the $d_{x,y}$ orbital: J_a represents

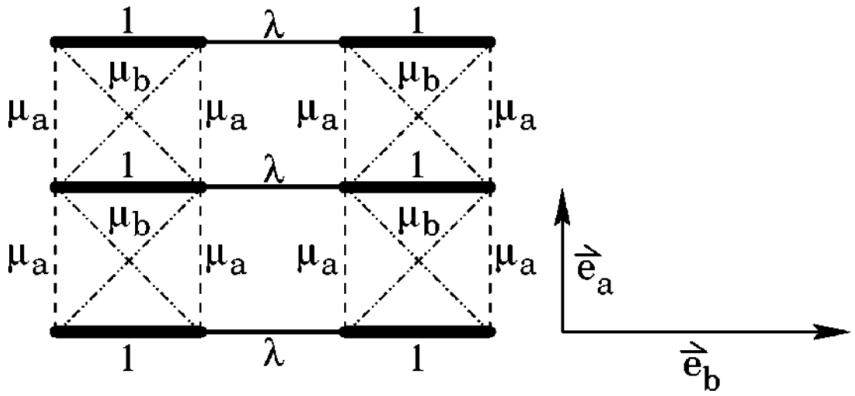

FIG. 7. Effective Lattice Model. γ denotes the two possible types of decoupled subsystems A,B. Taken from Ref. [28].

the path connecting V ions only separated along the $\hat{a}$ axis and J_b is path along the $\hat{a}$ axis and the $\hat{b}$ axis one ion spacing each. They are of comparable magnitude and can lead to frustration. Couplings in the c-direction seem to be of minor importance as experimental data shows [27].

A graphical representation of the resulting simplification of the VOPO-model is given in Figure 7. Its Hamiltonian takes the form

$$H_s = \sum_{\gamma=A,B} \sum_{i,j} \left(J_{1,\gamma} \boldsymbol{S}^1_{i,j} \boldsymbol{S}^2_{i,j} + J_{2,\gamma} \boldsymbol{S}^2_{i,j} \boldsymbol{S}^1_{i+1,j} + \sum_{m=1,2} [J_{a,\gamma} \boldsymbol{S}^m_{i,j} \boldsymbol{S}^m_{i,j+1} + J_{b,\gamma} \boldsymbol{S}^m_{i,j} \boldsymbol{S}^{m+1}_{i,j+1}] \right) \tag{38a}$$

$$= \sum_{\gamma=A,B} J_{1,\gamma} \sum_{i,j} \left(\boldsymbol{S}^1_{i,j} \boldsymbol{S}^2_{i,j} + \lambda_\gamma \boldsymbol{S}^2_{i,j} \boldsymbol{S}^1_{i+1,j} + \sum_{m=1,2} [\mu_{1,\gamma} \boldsymbol{S}^m_{i,j} \boldsymbol{S}^m_{i,j+1} + \mu_{2,\gamma} \boldsymbol{S}^m_{i,j} \boldsymbol{S}^{m+1}_{i,j+1}] \right), \tag{38b}$$

where γ denotes the separate subsystems, i, j the dimer, and m represents the left or right spin of a given dimer. $\boldsymbol{S}^m_{i,j}$ represent the usual spin operators. The second line expresses the Hamiltonian with coupling strengths relative to $J_{1,\gamma}$, namely the factors $\lambda_\gamma = J_{2,\gamma}/J_{1,\gamma}$, $\mu_{1,\gamma} = J_{a,\gamma}/J_{1,\gamma}$ and $\mu_{2,\gamma} = J_{b,\gamma}/J_{1,\gamma}$, which are all smaller than one.

4.3 Effective Hardcore Bosonic Hamiltonian

Starting from the effective Hamiltonian (38b) we now want to combine the two strongly coupled spins to one effective state. As a first step we transform our Hamiltonian into a form whose action on the tensor product basis of the total spin state is simple to work with. The triplet states of a single dimer could be written as

$$|0\rangle = |s\rangle = \frac{1}{\sqrt{2}}(|\uparrow\downarrow\rangle - |\downarrow\uparrow\rangle), \tag{39a}$$

$$-t^\dagger_{+,i,j} |0\rangle = |\uparrow\uparrow\rangle , \tag{39b}$$

$$t^\dagger_{-,i,j}\left|0\right\rangle = \left|\downarrow\downarrow\right\rangle, \tag{39c}$$

$$t^\dagger_{0,i,j}\left|0\right\rangle = \frac{1}{\sqrt{2}}(\left|\uparrow\downarrow\right\rangle + \left|\downarrow\uparrow\right\rangle), \tag{39d}$$

thereby relating them to the single spin states with respect to the component S_z. The singlet state is $|0\rangle = |s\rangle$ and the other three the excited triplet states, which we will interpret as different flavours of one hardcore boson. The creation operators $t^\dagger_{\alpha,i,j}$ on the left-hand side create such a triplon at site (i,j), where $\alpha \in \{+,-,0\}$ is treated like a flavor index. Since these excitations exclude one another they behave fermionic at the same side and bosonic at different sites, motivating the hardcore boson statistic.

With the definition of the triplon's creation and annihilation operators we can find the appropriate linear combinations to express the previously used spin-operators in the Hamiltonian. This allows us to bring the Hamiltonian into the form

$$H = H_0 + T_{-2} + T_{-1} + T_0 + T_1 + T_2, \tag{40}$$

where T_i are operators that change the number of triplons by i and H_0 represents the free triplon Hamiltonian. We find that the free Hamiltonian H_0 is given by

$$H_0 = \sum_{i,j} \boldsymbol{S}^1_{i,j}\boldsymbol{S}^2_{i,j} = \sum_{i,j}\sum_{\alpha\in\{+,-,0\}} \left(t^\dagger_{\alpha,i,j}t_{\alpha,i,j} - \frac{4}{3}\right). \tag{41}$$

Since all prefactors of the contributions of the T_i are smaller than one we can treat them with a perturbative approach as described in the next section. The change in the number of triplons can be at most two due to the structure of the perturbation terms, which act only on neighboring sites. In particular, the lowest state available is a double singlet and the highest a linear combination of triplon states. Since triplons are maximum angular momentum states, this difference adds up to two. For particle destruction the identity $T^\dagger_i = T_{-i}$ could be used to connect to the previous argument.

A systematic way to obtain a representation of the operators T_i is to calculate the matrix elements for specific dimer states like

$$\left\langle 0\right| x^\dagger_{i,j}x^\dagger_{i-1,j}x^\dagger_{i,j-1}H_{\text{int}}x_{i,j-1}x_{i-1,j}x_{i,j}\left|0\right\rangle \tag{42}$$

where $x_{i,j} \in \{\mathbb{1}, t^\dagger_{+,i,j}, t^\dagger_{0,i,j}, t^\dagger_{-,i,j}\}$ are triplon states of the dimer (i,j) and $H_{\text{int}} = H - H_0$.

4.4 Flow Equation

Since the Hamiltonian is not particle-conserving, we will first transform it into an effective particle-conserving model. A general scheme to find diagonal effective Hamiltonians at zero temperature is known as flow equations or continuously unitary transforms (CUT). This section will describe how CUTs could be applied in a relatively general form as given in Ref. [1] and later on how it could yield the wanted quantity for the given problem following the discussion in Ref. [29]. CUTs or the flow equation are used to find a systematic way to smoothly transform a given Hamiltonian into a diagonal form. This technique was invented by Wegner [30]. Since then many advanced forms have been developed like deepCUT, gCUT and epCUT[3, 2, 1]. In the following treatment, we will make additional assumptions beyond the most general setting for CUTs. The restrictions for our system are

- The unperturbed Hamiltonian H_0 has an equidistant spectrum of states,
- The perturbing Hamiltonian H_{int} only connects subspaces with a finite difference in particle number.

In this case a Hamiltonian can be written as in equation (40), if the maximal particle number difference is two, which we assume in the following. We now introduce the continuously transformed Hamiltonian as

$$H(l) = U(l)HU(l)^\dagger, \tag{43}$$

where $l \in \mathbb{R}$ is the so called flow parameter and $U(l)$ is a unitary operator. It should fulfill the requirements

$$H(0) = H_0 + T_{-2} + T_{-1} + T_0 + T_1 + T_2, \tag{44a}$$
$$H(\infty) = H_{\text{eff}}, \tag{44b}$$

where H_{eff} is the diagonal Hamiltonian we want to obtain with this transformation. It should be particle-conserving and therefore commute with the free Hamiltonian H_0. We want the operator $U(l)$ to be generated by the anti-hermitian generator $\eta(l)$ as

$$U(l) = Le^{\int_0^l \eta(l')dl'}, \tag{45}$$

where L denotes the l-ordering operator, which acts analogously to the well-known time ordering operator T. Taking the derivative of $H(l)$ with respect to l yields the so-called flow equation of the Hamiltonian $H(l)$, namely

$$\partial_l H(l) = [\eta(l), H(l)]. \tag{46}$$

In Wegner's original ansatz[30] the Hamiltonian $H = H_d + H_{\text{nd}}$ was separated into a diagonal part H_d and a non-diagonal part H_{nd}, with the generator

$$\eta(l)_{\text{Wegner}} = [H_d(l), H_{nd}(l)]. \tag{47}$$

This generator however has the unpleasant property to link subspaces of arbitrarily many particles. To conserve the particle count we introduce a different generator analogously to [1]. First we will introduce a more general representation for the Hamiltonian, which is given by

$$H(l) = H_0 + \sum_{k=1}^{\infty} \lambda^k \sum_{|m|=k} F(l;m)T(m), \tag{48}$$

where $F(l;m)$ are real-valued functions and we use the following notation for particle difference multiindices:

$$m = (m_1, m_2, m_3, \ldots, m_k), \tag{49}$$
$$m_i \in \{0, \pm 1, \pm 2\}, \tag{50}$$
$$|m| = k, \tag{51}$$
$$T(m) = T_{m_1} T_{m_2} \ldots T_{m_k}, \tag{52}$$

$$M(m) = \sum_i = 1^k m_i, \tag{53}$$

so that $H(l)$ expresses all possible combinations of the previously given T_m, $m \in \{0, \pm 1, \pm 2\}$ with its functional dependence on the flow parameter. This leads to a generator of the form

$$\eta(l) = \sum_{k=1}^{\infty} \sum_{|m|=k} \operatorname{sgn}(M(m)) F(l; m) T(m) \tag{54}$$

Using this as the starting point, we can find a nonlinear recursive differential equation system for the $F(l; m)$. It was solved and also shown that it preserves the restriction in connection of subspaces[1]. This means in the limit the Hamiltonian will take the form

$$H_{\text{eff}} = H_0 + \sum_{k=1}^{\infty} \lambda^k \sum_{|m|=k,\, M(m)=0} F(\infty; m) T(m), \tag{55}$$

where we truncate the the perturbation series in λ at finite order for practical calculations. Solutions for the coefficients up to order $k = 10$ are provided in [1], also describing their computer-aided solution for this problem. Here, we nevertheless want to obtain a free effective theory and find the appropriate dispersion relation.

4.5 Linked Cluster Calculations of the Dispersion Relation

Assuming we have brought our model for VOPO into the form (40) and have applied the CUT given above, we now have an effective Hamiltonian that preserves the particle number. In this paragraph, we will describe how we can obtain a dispersion relation from this intermediate result. In the case of our antiferromagnetic model the ground state is given by

$$|0\rangle := |\prod_i s_i\rangle \tag{56}$$

which is the product state of all singlet states of the dimers. The ground state of the full effective Hamiltonian is then given as

$$E_0 = \langle 0 | H_{\text{eff}} | 0 \rangle . \tag{57}$$

It is known from the linked cluster theorem that the finite order contribution of a short range interaction becomes independent of the cluster size if the size is large enough. This statement could be used to perform finite cluster calculations since our model only includes next-neighbor interactions. To obtain the dispersion relation we need to compute the dynamics of a single triplon. So we set our state to

$$|j\rangle = |s, s, \ldots, j, \ldots, s\rangle , \tag{58}$$

where the multiindex j denotes the dimer site and flavor of the excitation. Since the effective Hamiltonian conserves the particle number its action can only describe the excitation hopping to other sites. Therefore we can write

$$H_{\text{eff}} |j\rangle = J_1 \sum_i t_i |j + i\rangle , \tag{59}$$

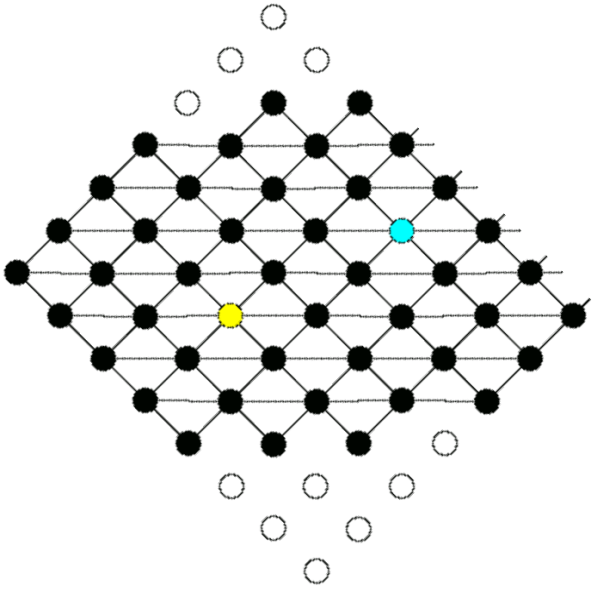

FIG. 8. This figure depicts a cluster for a hopping at order 8. Circles represent dimers, the yellow dot represents the starting point and the blue one the end point. All possible paths at the given order are represented by black circles and lines that mark the path. Taken from [29].

where J_1 is the dimer coupling constant and t_i are real-valued coefficients with a multiindex i labeling the corresponding hopping site. The coefficients t_i can again be calculated by finite cluster calculations. A cluster for hopping of order 8 is depicted in Figure 8. Once we have the coefficients t_i we can obtain the dispersion relation by a fourier transform as

$$\omega(\boldsymbol{k}) = \frac{J}{\sqrt{N}} \sum_{\boldsymbol{j}} t_{\boldsymbol{j}} \exp\left(i\boldsymbol{j}\boldsymbol{k}\right). \tag{60}$$

Here we used the previously suppressed vector notation for clarity. In Reference [28] and [31] this scheme was used up to third order in the inter-dimer coupling. The results for the hopping elements are given by

$$t_{00} = 1 - \lambda^2/16 + 3\lambda^3/64 + 3\mu_-^2/4 + 3\mu_-^2\mu_+/8, \tag{61}$$
$$t_{01} = \mu_-/2 - \mu_-^3/8 - 5\lambda^2\mu_-^2/32, \tag{62}$$
$$t_{02} = -\mu_-^2/8 - \mu_-^2\mu_+/8, \tag{63}$$
$$t_{03} = \mu_-^3/16, \tag{64}$$
$$t_{10} = -\lambda/4 - \lambda^2/8 + \lambda^2/64 + \lambda\mu_-^2/16, \tag{65}$$
$$t_{11} = \lambda\mu_-/8 - \lambda^2\mu_-/32 + \lambda\mu_-\mu_+/16, \tag{66}$$
$$t_{12} = -3\lambda\mu_-^2/32, \tag{67}$$
$$t_{20} = -\lambda^2/32 - \lambda^3/64, \tag{68}$$
$$t_{21} = 3\lambda^2\mu_-/64, \tag{69}$$
$$t_{30} = -\lambda^3/128, \tag{70}$$

where $\lambda = J_{1,\gamma}/J_{2,\gamma},\ \mu_- = (J_{a,\gamma} - J_{b,\gamma})/J_{1,\gamma}),\ \mu_+ = (J_{a,\gamma} + J_{b,\gamma})/J_{1,\gamma})$. We split the multiindex into the first index representing the dimer bond and the second the corresponding chain. Since only the difference counts we set the position to zero for convenience. Because we have a simple square lattice shape in dimer representation we obtain for the dispersion relation

$$\omega(\boldsymbol{k}) = J \sum_{ij} 2^{2-\delta_{i0}-\delta_{j0}} t_{ij} \cos(ik_y) \cos(jk_x). \tag{71}$$

4.6 Fit to Experimental Data

Since we started with a model with unspecified coupling constants we now need to fit them to the experimental data from inelastic neutron scattering. This was done with the square $\omega^2(q)$ since it has a smoother form. The parameter $\mu_{+,\gamma}$ can be fixed using the maximum of the measured susceptibility $\chi_{\max}$ instead of being fitted [31]. This leads to the coupling coefficients [31]

$$(J_{1A}, J_{2A}, J_{aA}, J_{bA}) = (144.9K, 95.5K, 11.6K, 16.4K), \tag{72}$$

$$(J_{1B}, J_{2B}, J_{aB}, J_{bB}) = (122.9K, 95.0K, 13.4K, 18.6K). \tag{73}$$

For further details refer to [31, 28]. The fitted coupling constants are all it takes to derive the free pure hardcore bosonic behavior of the system. For example these values lead to a gap energy of the dispersion relation of about 45 K. Beside this the effective Hamiltonian yielded by the CUT could be used as a starting point to include further interactions of the system. For further information refer to [32]. This was done on a mean field level for Cs_2CuCl_4[21] and in one dimension for $BaCu_2V_2O_8$[33] even within the same perturbation order as the later outlined Brückner approach in chapter 5.

5 Brückner Approach

In this chapter, we will outline the Brückner method for the calculation of the spectral representation for the propagator in a free model of hardcore bosons with a single gapped ground state and unbroken flavour symmetry. The name comes from the well-known method for treating nuclear matter [34], but it has also been applied to spin systems by Sushkov et al. [35], but at zero temperature to deal with quantum fluctuations. We will instead use it to account for the effects of thermal fluctuations, which complicate the description of the propagator at finite temperatures. This chapter follows the discussion of Fauseweh et al.[8, 7]. To use this approach in a more general setting a diagonalization with respect to flavor space needs to be applied. In the first section, we will discuss the treatment of hardcore bosons though bosons with finite repulsion. In the second and third section, we use the Brückner approach to derive the spectral function of the propagator and the self energy to first order in $e^{\beta\Delta^\alpha}$, where Δ^α is the gap of the dispersion relation of the hardcore excitation. We will then extend this framework by using full propagators in a self-consistent iteration. Finally we will give some remarks on how to implement this approach algorithmically.

5.1 Bosonic Ansatz with Infinite Repulsion

We will treat the free hardcore boson model by a bosonic ansatz which has the form

$$H = H_0 + U \sum_{i,\alpha,\beta} b^\dagger_{i,\alpha} b^\dagger_{i,\beta} b_{i,\beta} b_{i,\alpha}, \tag{74}$$

where U is a positive interaction strength and all operators in the given equation should be interpreted as regular bosonic operators. H_0 is the initial Hamiltionian and the last term is an on-site local interaction, where we will later take the limit $U \to \infty$. This repulsion acts between all possible flavored excitations. The idea is that if we take the limit for the occupation of multiply occupied state to infinity, regardless of flavor, the hardcore constraint will be retrieved. We first consider this theory and only afterwards take the limit to infinity in order to avoid the more complicated commutator and Wick's theorem of hardcore bosons. However, a regular perturbation theory in U will fail in this limit. For this reason we select a different parameter in the next paragraph.

Perturbation Parameter We use a bosonic perturbation theory as given in the book [36]. The main object we have to deal with is the Greens-function of the form

$$G^\alpha(j,\tau) = -\langle T b^\dagger_{j,\alpha}(-i\tau) b_{0,\alpha}(0)\rangle \quad \tau \in \mathbb{R}. \tag{75}$$

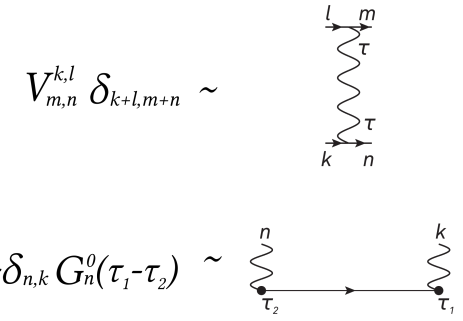

FIG. 9. Feynman rules of interaction vertex and bare boson propagator

We assume to have an infinite lattice and therefore describe the problem in momentum-space by using Fourier transforms. For the free bosonic propagator $G_k^{0,\alpha}$ in momentum space this yields

$$G_k^{0,\alpha}(\tau) = \begin{cases} -\exp(-\tau\omega(k))(1+\langle n_k^\alpha\rangle_0) & \text{for } \tau > 0 \\ -\exp(-\tau\omega(k))\langle n_k^\alpha\rangle_0 & \text{for } \tau \leq 0, \end{cases} \tag{76}$$

where $\langle n_k^\alpha\rangle_0$ denotes $\langle b_k^{\dagger,\alpha} b_k^\alpha\rangle_0$, the expectation value of the occupation of a momentum state k with respect to the Hamiltonian H_0. The property of interest is the behavior of this function in the limit of low temperature:

$$\langle n_k^\alpha\rangle_0 = \frac{1}{e^{\beta\omega^\alpha(k)}-1} \overset{\beta\gg 0}{\approx} e^{-\beta\omega^\alpha(k)}. \tag{77}$$

If there is a finite gap, the propagator going backward in imaginary time are suppressed by at least $e^{-\beta\Delta^\alpha}$ where Δ^α represents the gap. With this we found our perturbation parameter that is small in the low temperature regime.

5.2 Calculation of the Propagator

To calculate the full propagator, we need to sum up all diagrams with two external legs that contribute to first order. Since we saw that propagators going backwards in imaginary time are suppressed with our expansion parameter, we can drop diagrams with more than one of these. The Hartree- and Fock-diagrams in Figure 10 clearly contribute, the other diagrams are just the two types represented in Figure 11. These are the only possible types of diagrams at this order: Since we have just one propagator going in and one coming out of each diagram, all other need to be connected in a loop. Suppose all propagators are lined up, then there always needs to be one propagator running back in time as in the case of the mentioned types of diagrams. But since we restrict ourselves to just one propagator going backwards in imaginary time, there could be no additional diagram type but the ones already considered.

On the other hand, it is immediately clear that we cannot stick to any finite set of diagrams, since these types of diagrams have in principle arbitrarily many large couplings. We will sum up these contributions using an implicit calculation. To do

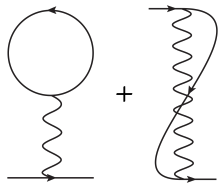

FIG. 10. Hartree- and Fock-Diagram

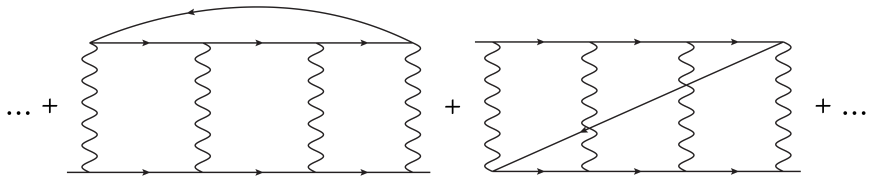

FIG. 11. Representatives of two types of diagrams in first order of the perturbation theory.

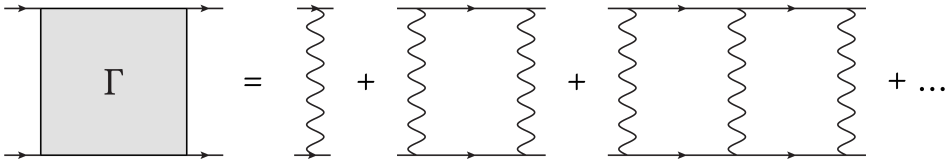

FIG. 12. Scattering amplitude diagrams that contribute to the propagator in first order

this, we first consider the scattering amplitude $\Gamma^{\alpha}(P,K,Q)$, depicted in Figure 12. We have introduced the notations $P=(p,i\omega_p)$ to combine momenta and frequencies. The dependencies P,K,Q represent the independent frequencies and momenta in a scattering of two excitations. The Bethe Salpeter equation relates the scattering amplitude and the propagator through

$$\Gamma^{\alpha,\beta}(P,K,Q)=\frac{U}{N\beta}-\frac{U}{N\beta}\sum_{L}\Gamma^{\alpha,\beta}(P,K,Q)G_0^{\alpha}(P+L)G_0^{\beta}(-L), \tag{78}$$

which is shown in Figure 14. The negative sign in front of the second term is generated by the Feynman rules and the fact that the term represents a contribution of one order higher in the coupling interaction than the bare scattering amplitude.

We now give an argument that the scattering amplitude only depends on the total momentum P, which simplifies the problem dramatically. First we consider the diagram with two propagator lines shown in Figure 13 which is the first diagram that can depend on more than the total momentum P. We translate it into an mathematical form as

$$-\frac{U^2}{\beta^2}\sum_{L}G_0^{\alpha}(P+L)G_0^{\beta}(-L). \tag{79}$$

Since the interaction does not depend on the momentum, this depends on neither K nor Q. Therefore both the diagrams with one and two vertices don't depend on anything

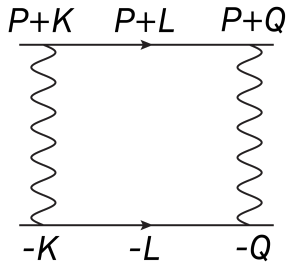

FIG. 13. Diagrams with two propagator in first order of the perturbation theory

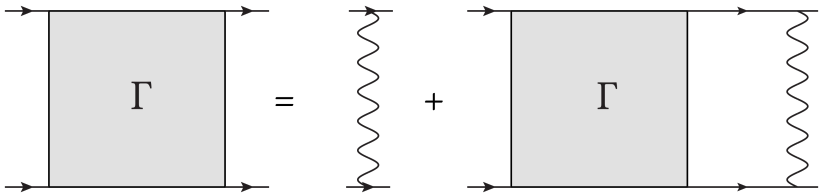

FIG. 14. Bethe Salpeter Equation

else than P. Because all the rest of the diagrams are concatenations of these types of diagrams, the complete statement is a consequence of mathematical induction.

Taking this simplification into account we can easily calculate by basic algebra that

$$\Gamma^{\alpha,\beta}(P) = \frac{U/(N\beta)}{1 + UM^{\alpha,\beta}(P)} \tag{80}$$

holds, where we introduced the function

$$M^{\alpha,\beta}(P) := \frac{1}{N\beta} \sum_{L} G_0^{\alpha}(P+L) G_0^{\beta}(-L). \tag{81}$$

It is handy to represent this quantity by a Hilbert representation

$$M^{\alpha,\beta}(\omega, p) =: \int_{-\infty}^{\infty} \frac{\rho_p^{\alpha,\beta}(x)}{\omega - x} dx. \tag{82}$$

This representation exists because $M(P)$ is a convolution of two greens-functions and therefore is at least of order $O(\frac{1}{\omega})$. We now employ the Matsubara technique: Inserting the bare bosonic propagator in the Matsubara-representation

$$G_0^{\alpha}(P) = \frac{1}{i\omega_p - \omega^{\alpha}(p)} \tag{83}$$

into equation (81) yields

$$M^{\alpha,\beta}(\omega, p) = \frac{1}{N\beta} \sum_{l, i\omega_l} \frac{1}{i(\omega_p + \omega_l) - \omega^{\alpha}(p+l)} \frac{1}{i\omega_{-l} - \omega^{\beta}(-l)}. \tag{84}$$

Since we want to apply our approach to a situation in which the excitations are degenerated, we now drop the index of the dispersion $\omega(l) = \omega^\alpha(l)$ to avoid a cluttered notation. We use a common trick from complex analysis to integrate rather than sum over the Matsubara-frequencies. For this we introduce a function $h(z) := \frac{1}{e^{\beta z}-1}$ which has a simple pole at the position of the Matsubara-frequencies. Applying the residue theorem to the simple closed curve γ as shown in Figure 15 we obtain

$$M^{\alpha,\beta}(P) = \frac{1}{2\pi i}\int_\gamma h(z)\frac{1}{N}\sum_l \frac{1}{i\omega_p + z - \omega(p+l)}\frac{1}{-z-\omega(-l)}dz, \tag{85}$$

This equation also differs by a factor $\frac{1}{\beta}$ which is hidden in the residue as

$$e^{\beta x} \overset{x\approx i\omega_p}{=} 1 + \beta(x - i\omega_p) + O((x - i\omega_p)^2). \tag{86}$$

We exploit the fact that the function vanishes for $\omega \to \infty$: This could be used to wrap the path of the integral around the other two poles that don't reside on the imaginary axis by tearing the loop apart in infinity. A sign flip results from reversing the path orientation from counterclockwise to clockwise.

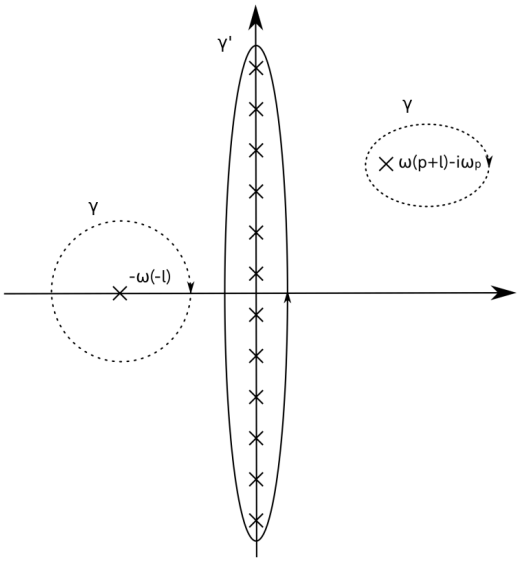

FIG. 15. Path transformation from the (solid) path around the Matsubara poles to the (dotted) paths around the propagator poles for $M(P)$.

Using the new curve we find after some algebra that

$$M^{\alpha,\beta}(P) = \frac{1}{N}\sum_l \frac{1}{i\omega_p - [\omega(-l) + \omega(p+l)]} \cdot \left(\frac{1}{e^{-\beta\omega(-l)}-1} - \frac{1}{e^{\beta\omega(p+l)}-1}\right) \tag{87}$$

holds. Using the Dirac identity

$$\int_{\mathbb{R}} \frac{1}{x - (\omega + i0^+)} = \mathcal{P}\left[\frac{1}{x-\omega}\right] - \int_{\mathbb{R}} i\pi\delta(x-\omega), \tag{88}$$

and taking the limit $\rho_p^{\alpha,\beta}(x) = -\frac{1}{\pi}\mathrm{Im}\left[\lim_{i\omega_p \to x+i\delta} M^{\alpha,\beta}(\omega_p, p)\right]$ we get

$$\rho_p^{\alpha,\beta}(x) = -\frac{1}{N}\sum_l \delta\left(x - [\omega(-l) + \omega(p+l)]\right) \cdot \left(\frac{1}{e^{\beta\omega(p+l)} - 1} - \frac{1}{e^{-\beta\omega(-l)} - 1}\right), \quad (89)$$

so that $\rho_p^{\alpha,\beta}(x)$ is always negative. Since it has a constant contribution, there exists no spectral representation for $\Gamma(P)$ and it is also not possible to take the limit of $U \to \infty$ because we know no reasonable expansion in $1/U$. Instead we consider an object that has a spectral representation by eliminating the constant part in $\Gamma(P)N\beta$. Since $\frac{U}{1+UM^{\alpha,\beta}(\omega,p)} - U \overset{|w|\gg 1}{\propto} \frac{1}{\omega}$, we can define $\bar{\rho}_p^{\alpha,\beta}$ through

$$\frac{U}{1 + UM^{\alpha,\beta}(\omega, p)} - U = \int_{-\infty}^{\infty} \frac{\bar{\rho}_p^{\alpha,\beta}(x)}{\omega - x} dx. \quad (90)$$

The left-hand side has a pole since $M^{\alpha,\beta}$ is negative for $\omega \approx U$ and $\rho_p^{\alpha,\beta}$ is negative. This is an anti-bound scattering state. It will leave an important trace even after taking the limit of $U \to \infty$ which we discuss later. First off, we will calculate the spectral function as before and later on take a closer look at additional contributions that turn out to be of major importance. Using the Dirac-identity we get

$$-\frac{1}{\pi}\lim_{\omega \to x+i\delta} \mathrm{Im}\left[\frac{U}{1 + UM^{\alpha,\beta}(\omega, p)} - U\right] \quad (91)$$

$$\overset{(88)}{=} -\frac{1}{\pi}\mathrm{Im}\left[\frac{U}{1 + U\left(-i\pi\rho_p^{\alpha,\beta}(x) + \mathcal{P}\int_{-\infty}^{\infty} \frac{\rho_p^{\alpha,\beta}(y)}{x-y} dy\right)} - U\right] \quad (92)$$

$$= \frac{-U^2\rho_p^{\alpha,\beta}(x)}{\left[1 + U\mathcal{P}\int_{-\infty}^{\infty} \frac{\rho_p^{\alpha,\beta}(y)}{x-y} dy\right]^2 + \left[U\rho_p^{\alpha,\beta}(x)\pi\right]^2} \quad (93)$$

Now we can take the limit in a reasonable way and define for $U \to \infty$ the new function

$$f_p^{\alpha,\beta}(x) := \frac{-\rho_p^{\alpha,\beta}(x)}{\left[\mathcal{P}\int_{-\infty}^{\infty} \frac{\rho_p^{\alpha,\beta}(y)}{x-y} dy\right]^2 + \left[\rho_p^{\alpha,\beta}(x)\pi\right]^2}. \quad (94)$$

To understand the limit better we investigate what happens for $\omega \approx U$. With the help of the Laurent series

$$\frac{1}{\omega - x} = \frac{1}{\omega}\frac{1}{1 - \frac{x}{\omega}} \quad (95)$$

$$\overset{|\omega|>|x| \Longrightarrow |\frac{x}{\omega}|<1}{=} \frac{1}{\omega}\sum_{k=0}^{\infty}\left(\frac{x}{\omega}\right)^k, \quad (96)$$

we approximate M for the case $\omega \approx U$, which is reasonable since $\rho_p(x)$ has a compact support with respect to x as one can see from the δ-functions. So we use this

approximation to write the term in the form

$$\frac{U}{1+UM^{\alpha,\beta}(\omega,p)} - U \approx \frac{U}{1+U\rho_0^{\alpha,\beta}(p)\frac{1}{\omega}+U\rho_1^{\alpha,\beta}(p)\frac{1}{\omega^2}} - U \tag{97}$$

Here we introduced the weight and first moment of ρ_p as

$$\rho_0^{\alpha,\beta}(p) = \int_{-\infty}^{\infty} \rho_p^{\alpha,\beta}(x)dx, \tag{98}$$

$$\rho_1^{\alpha,\beta}(p) = \int_{-\infty}^{\infty} x\rho_p^{\alpha,\beta}(x)dx. \tag{99}$$

At this stage, the function $\rho_0^{\alpha,\beta}$ is a constant, because integrating $\rho^{\alpha,\beta}$ cancels the δ-function in equation (89) and leaves two independent summations. One is a shifted Bose function and the other a Bose function with a negative argument. Summing over all momentums yields a constant. This will change when we take a dressed propagator into account. Again we employ the usual trick to calculate the new contribution to $\bar{\rho}^{\alpha,\beta}$.

$$\frac{-1}{\pi}\lim_{\omega\to x+i\delta}\mathrm{Im}\left[\frac{U\omega^2}{\omega^2+U\rho_0^{\alpha,\beta}\omega+U\rho_1^{\alpha,\beta}(p)}\right] \tag{100}$$

$$=\frac{-U}{\pi}\lim_{\omega\to x+i\delta}\mathrm{Im}\left[\frac{\omega^2}{(\omega-\omega_1^{\alpha,\beta})(\omega-\omega_2^{\alpha,\beta})}\right] \tag{101}$$

Where we introduced the short hand notation

$$\omega_1^{\alpha,\beta} := -\frac{U\rho_0^{\alpha,\beta}}{2} + \sqrt{\frac{U^2(\rho_0^{\alpha,\beta})^2}{4} - U\rho_1^{\alpha,\beta}(p)}, \tag{102}$$

$$\omega_2^{\alpha,\beta} := -\frac{U\rho_0^{\alpha,\beta}}{2} - \sqrt{\frac{U^2(\rho_0^{\alpha,\beta})^2}{4} - U\rho_1^{\alpha,\beta}(p)}. \tag{103}$$

In the following we will also drop the flavor indices for ω_1 and ω_2. Investigating the behavior of these frequencies we notice that $\omega_1^{\alpha,\beta}$ scales with $\mathcal{O}(U)$ but $\omega_2^{\alpha,\beta}$ scales with $\mathcal{O}(U^0)$, considering that $\rho_0^{\alpha,\beta}$ is negative since $\rho^{\alpha,\beta}$ is also negative. Carrying on with the help of the Dirac-identity and the partial fraction decomposition

$$\frac{x^2}{(x-\omega_1)(x-\omega_2)} = \frac{\omega_1^2}{(\omega_1-\omega_2)}\frac{1}{(x-\omega_1)} + \frac{\omega_2^2}{(\omega_2-\omega_1)}\frac{1}{(x-\omega_2)} \tag{104}$$

we conclude that (101) is equal to

$$U\left(\frac{\omega_1^2}{\omega_1-\omega_2}\delta(x-\omega_1) + \frac{\omega_2^2}{\omega_2-\omega_1}\delta(x-\omega_2)\right). \tag{105}$$

Since we are interested in the limit of $U\to\infty$, the pole at ω_2 becomes unreasonable because the expansion at this value in frequency space is unreasonable as well and we sought for neglected contributions by taking the limit at this step. Therefore they should disappear in the limit. Because of this ω_2 could be interpreted as an artifact of

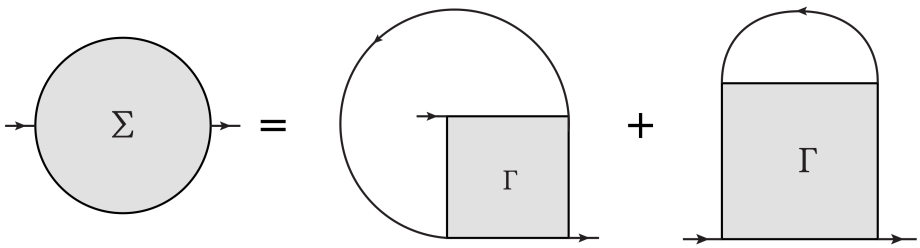

FIG. 16. Relation of the self energy and the scattering amplitude

the expansion and will be dropped out of the calculation. The complete contribution to $\bar{\rho}$ is then given by

$$\bar{\rho}_p^{\alpha,\beta}(x) = f_p^{\alpha,\beta}(x) + U\left(\frac{\omega_1^2}{\omega_1 - \omega_2}\delta(x-\omega_1)\right). \tag{106}$$

The next step is to calculate the self energy and find out where the high energy anti-bound state leaves traces if we take the limit $U \to \infty$.

5.3 Calculation of the Self Energy

The definition of the self energy Σ^α with respect to one loop contributions in the first order of our approximation is represented in Figure 16. Since we have to deal with multiple flavors there is one important difference in the two types of diagrams. The Fock-like diagrams have a propagator line which connects to all propagators and since we have no interaction that interconnects different flavors, all propagator are associated with the same flavor. In the case of the Hartree-like diagram type there is an independent loop instead. This loop can in fact have a propagator line for every flavor. Therefore we have two diagrams with different multiplicities. As an equation it reads

$$\Sigma^\alpha(P) = \frac{-1}{\beta N}\sum_\alpha \sum_K (1+\delta_{\alpha,\beta}) G_0^\beta(K) e^{i\omega_k 0^+} \Gamma^{\alpha,\beta}(P+K) \tag{107}$$

The convergence factor is needed for propagation at the same imaginary time as in the Hartree-contribution. Taking into account that the degeneracy causes all propagators $G^\alpha(P) = G(P)$ and their spectral function to be equal, we can conclude

$$\Sigma^\alpha(P) = \frac{-(1+N_f)}{\beta N}\sum_K G_0^\beta(K) e^{i\omega_k 0^+} \Gamma^{\alpha,\beta}(P+K). \tag{108}$$

Since we have now accounted for the flavor indices, and the rest of the calculation is indifferent with respect to them, we suppress them on the right hand side of the equations. Inserting the equation for $\Gamma(P)$ yields

$$\Sigma^\alpha(P) = -2\sum_K G_0(K) e^{i\omega_k 0^+} \frac{U}{1+UM(P+K)}. \tag{109}$$

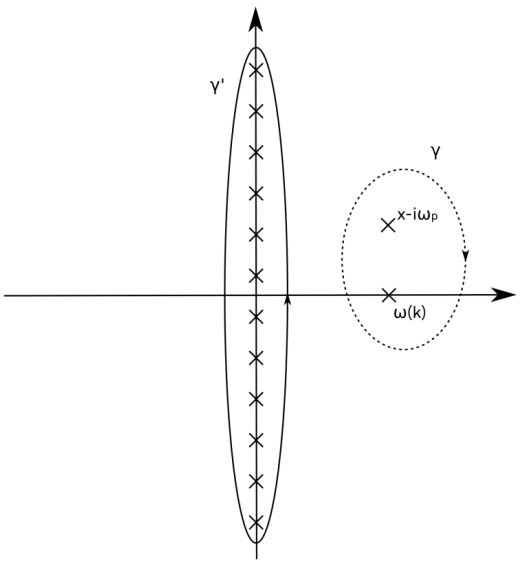

FIG. 17. Poles in the complex plain of the self energy and integration paths

Now we insert the spectral function including the contribution from the Hartree-Fock diagram:

$$\Sigma^{\alpha}(P) = \frac{-(1+N_f)}{N\beta}\sum_K G_0(K)e^{i\omega_k 0^+}\left(\int_{-\infty}^{\infty}\frac{\bar{\rho}_{p+k}(x)}{i\omega_p + i\omega_k - x}dx + U\right). \tag{110}$$

Evaluating the last term by carrying out the Matsubara summation in the same form as before yields

$$\Sigma^{\alpha}(P) = \frac{-(1+N_f)}{N\beta}\sum_K G_0(K)e^{i\omega_k 0^+}\left(\int_{-\infty}^{\infty}\frac{\bar{\rho}_{p+k}(x)}{i\omega_p + i\omega_k - x}dx\right) + \frac{2}{N}\sum_k \frac{U}{e^{\beta\omega(k)}-1}. \tag{111}$$

Once again we need to calculate the Matsubara-summation transformed to an integration along the path depicted in Figure 17. We also exploited again the fact that the spectral function vanishes for large frequencies to transform the integral into a summation over two residues. A simple calculation which yields

$$\frac{-(1+N_f)}{N\beta}\sum_K \frac{1}{i\omega_k - \omega(k)}e^{i\omega_k 0^+}\int_{-\infty}^{\infty}\frac{\bar{\rho}_{p+k}(x)}{i\omega_p + i\omega_k - x}dx \tag{112}$$

$$= \frac{(1+N_f)}{N}\sum_k \int_{-\infty}^{\infty}\left(\frac{\bar{\rho}_{k+p}(x)}{i\omega_p - (x-\omega(k))}\left[\frac{1}{e^{\beta\omega(k)}-1} - \frac{1}{e^{\beta x}-1}\right]\right)dx \tag{113}$$

Next we replace $\bar{\rho}$ with the expression (130) and cancel one integration with the δ-function. This yields

$$\Sigma^{\alpha}(P) = \frac{(1+N_f)}{N}\sum_k \frac{U}{e^{\beta\omega(k)}-1} + \frac{2}{N}\sum_k \int_{-\infty}^{\infty}\frac{f_{k+p}(x)}{i\omega_p - (x-\omega(k))}\left[\frac{1}{e^{\beta\omega(k)}-1} - \frac{1}{e^{\beta x}-1}\right] \tag{114}$$

FIG. 18. Dyson Equation

$$+\frac{2}{N}\sum_k U\left(\frac{\omega_1^2}{\omega_1-\omega_2}\right)\frac{1}{i\omega_p-(\omega_1-\omega(k))}\left[\frac{1}{e^{\beta\omega(k)}-1}-\frac{1}{e^{\beta\omega_1}-1}\right]. \tag{115}$$

The last term of this equation still depends on U explicitly and implicitly in the variables ω_1 and ω_2, so we try to find an expansion in $1/U$ to identify a reasonable limit for this expression. We find

$$U\left(\frac{\omega_1^2}{\omega_1-\omega_2}\right)\frac{1}{i\omega_p-(\omega_1-\omega(k))}=U\left(-1+\left[\frac{i\omega_p}{\rho_0}-\frac{\rho_1(p+k)}{\rho_0^2}+\frac{\omega(k)}{\rho_0}\right]\frac{1}{U}+\mathcal{O}\left(\frac{1}{U^2}\right)\right). \tag{116}$$

The only part that diverges as $U\to\infty$ cancels out in the equation for the self energy since we previously added this contribution, the Hartree-Fock-term, to define the spectral function. So we are now safe to take the limit $U\to\infty$. As we have a complete description of the self energy we are now able to use the Dyson equation to obtain the dressed propagator up to the given order in our perturbation approach. The Dyson equation is given in graphical form in Figure 18. From this equation we retrieve our spectral function as

$$A^\alpha(\rho,\omega)=\frac{-1}{\pi}\mathrm{Im}\lim_{i\omega_p\to\omega+i\delta}G^\alpha(i\omega_p) \tag{117}$$

$$=\frac{-1}{\pi}\frac{\mathrm{Im}[\Sigma^\alpha(\omega,p)]}{[\omega-\omega(p)-\mathrm{Re}[\Sigma^\alpha(\omega,p)]]^2+[\mathrm{Im}[\Sigma^\alpha(\omega,p)]]^2}. \tag{118}$$

For this calculation we split the self energy into its real and imaginary part. The strongest influence on the position of the peak comes from the real part of the self energy while the imaginary part mainly influences the width. A simple calculation using the Dirac-identity and equation (88) yields

$$\mathrm{Re}[\Sigma^\alpha(\omega,p)]=\frac{(1+N_f)}{N}\sum_k\left[\frac{\omega}{\rho_0}-\frac{\rho_1(p+k)}{\rho_0^2}+\frac{\omega(k)}{\rho_0}\right]\frac{1}{e^{\beta\omega(k)}-1} \tag{119}$$

$$+\mathcal{P}\int_{-\infty}^{\infty}\frac{\rho_{\Sigma,p}(x)}{\omega-x}dx$$

$$\mathrm{Im}[\Sigma^\alpha(\omega,p)]=-\pi\rho_{\Sigma,p}(\omega). \tag{120}$$

Here we introduced the spectral function of the self energy in the usual manner. By a simple application of the Dirac identity, it is given as

$$\rho^\alpha_{\Sigma,p}(\omega)=\frac{(1+N_f)}{N}\sum_k f_{k+p}(\omega+\omega(k))\left[\frac{1}{e^{\beta\omega(k)}-1}-\frac{1}{e^{\beta(\omega+\omega(k))}-1}\right]. \tag{121}$$

Now we finally have all information to calculate the spectral function for a given dispersion relation within the accuracy of our perturbation theory. In the next section we are going to extend the diagrams we accounted for to diagrams with dressed propagators. This opens the opportunity to include also higher order contributions in a non-perturbative fashion.

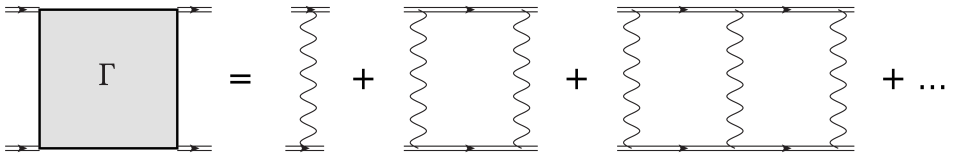

FIG. 19. The dressed scattering amplitude

5.4 Selfconsistent Extension

In this section we are going to extend the previously derived diagrams to dressed diagrams. For the bosonic case it is known that this kind of selfconsistent approach can predict the conservation of certain quantities like the particle number correctly[37]. This approach will lead us to a selfconsistent iteration scheme that has proven superior to the non-selfconsistent approach. The general idea is to replace the bare propagator with dressed ones in every diagram. This is possible since all presented diagrams are skeleton diagrams[36] and therefore we don't overcount any diagrams. The first affected diagram is the diagram of the scattering amplitude, depicted in Figure 21. This yields

$$\Gamma^{\alpha,\beta}(P,K,Q) = \frac{U}{N\beta} - \frac{U}{N\beta}\sum_{L}\Gamma^{\alpha,\beta}(P,K,Q)G^{\alpha}(P+L)G^{\beta}(-L). \tag{122}$$

Since we don't know the exact solution for the full propagator we replace it by its density

$$G^{\alpha}(j,\tau) =: \int_{-\infty}^{\infty}\frac{A^{\alpha}(x)}{\omega - x}dx. \tag{123}$$

This leads to the modified expression for

$$M^{\alpha,\beta}(P) = \frac{1}{N}\sum_{l}\int_{-\infty}^{\infty}\int_{-\infty}^{\infty}dxdx'\frac{A_{p+l}(x)A_{-l}(x')}{i\omega_p - (x'+x)}\left(\frac{1}{e^{-\beta x'}-1} - \frac{1}{e^{\beta x}-1}\right). \tag{124}$$

As a next step we want to compute the Matsubara summation by turning over to the spectral representation with the help of the Dirac-identity as before. This results in

$$\rho_p^{\alpha,\beta}(y) = \frac{-1}{N}\sum_{l}\int_{-\infty}^{\infty}dx\left(\frac{A_l(x)}{e^{\beta x}-1}A_{p-l}(y-x) - A_l(x)\frac{A_{p-l}(y-x)}{e^{-\beta(y-x)}-1}\right). \tag{125}$$

The delta function binds the two integrations into an single convolution. In total we now have to calculate two convolutions, one with respect to frequencies and the other with respect to momentum. The next step in the non-selfconsistent calculation is to derive the representation of $f_p(x)$. Since the complete calculation relies solely on the spectral function $\rho_p(x)$ and no special assumption about its properties have been made, the result is the same with respect to the function $\rho_p(x)$. It is given in equation (94), but has to be interpreted with the spectral function given in (125). In addition the discussion of the additional pole of spectral function $\bar{\rho}$ stays the same. The only problem that might arise is that we don't know if ρ has a compact support, but the application of the technique does not show that this is a problem. In general all spectral functions can have long tails in frequency space. Another difference is that

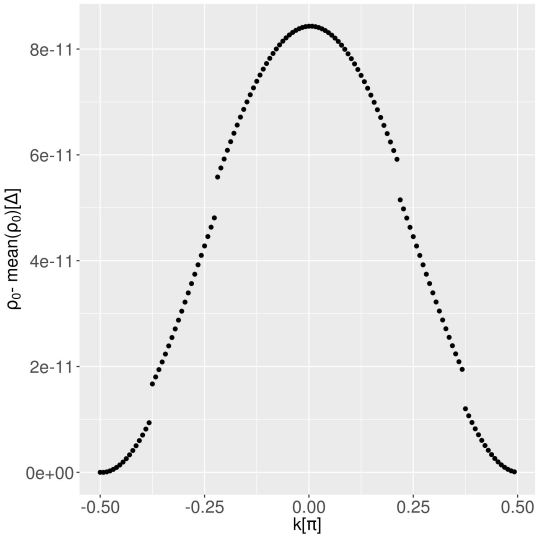

FIG. 20. ρ_0 fluctuations for a spin ladder model in 1D with next neighbor hopping. The dispersion has a gap energy $\Delta = 1$ and bandwidth $W = 0.5\Delta$ at 1 K. The used resolution is 16384 frequency and 128 momentum mesh points.

$\rho_0(p)$ also depends on momentum, since the previous argument no longer holds. On the other hand we can consider it to be approximately constant for another reason. Assuming the sum rule $\int_{-\infty}^{\infty} A(x,k)dx = 1-(1+N_f)n(T) =: C(T)$ holds, which clearly should be the case in the low temperature limit, if our approximation is right. We now exploit a property of the integral convolution $*$ related to the Fubini theorem which reads

$$\int_{\mathbb{R}} (f * g)(x)dx = \left(\int_{\mathbb{R}} f(x)dx\right)\left(\int_{\mathbb{R}} g(x)dx\right). \tag{126}$$

Using this property in combination with the sum rules yields

$$\int_{\mathbb{R}} \rho_p^{\alpha,\beta}(y) = \frac{-1}{N}\sum_l \int_{-\infty}^{\infty} dx \left(\frac{A_l(x)}{e^{\beta x}-1}C(T) - C(T)\frac{A_l(x)}{e^{-\beta x}-1}\right). \tag{127a}$$

$$= -(n(T)C(T) - C(T)\tilde{n}(T)). \tag{127b}$$

In the last line we used the fact that $C(T)$ is independent of l, resulting in a simple summation, as well as

$$n(T) = \frac{1}{N}\sum_k n_k := \frac{1}{N}\sum_k \int_{-\infty}^{\infty} A_k(x)\frac{1}{e^{\beta x}-1}, \tag{128}$$

$$\tilde{n}(T) := \frac{1}{N}\sum_k \tilde{n}_k = \frac{1}{N}\sum_k \int_{-\infty}^{\infty} A_k(x)\frac{1}{e^{-\beta x}-1}. \tag{129}$$

We therefore expect ρ_0 to approximately be a temperature-dependent constant. Numerical data seem to support this argument as well as shown in Figure 20. Similar tricks might yield interesting relations for ρ_1 as well.

The full expression for $\bar{\rho}$ now reads

$$\bar{\rho}_p^{\alpha,\beta}(x) = f_p(x) + U\left(\frac{\omega_1(p)^2}{\omega_1(p)-\omega_2(p)}\delta(x-\omega_1(p))\right), \tag{130}$$

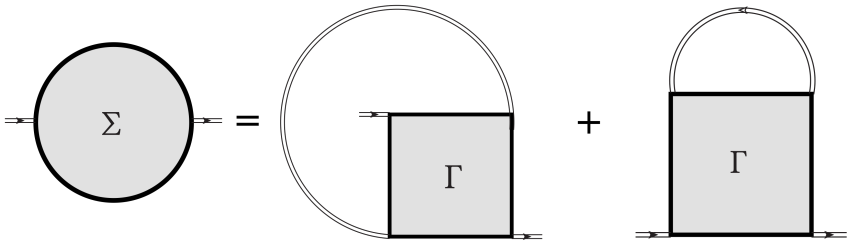

FIG. 21. The dressed Self Energy Diagram

where we defined the two poles in a similar fashion as before by

$$\omega_1(p) := -\frac{U\rho_0(p)}{2} + \sqrt{\frac{U^2\rho_0^2(p)}{4} - U\rho_1(p)}, \tag{131}$$

$$\omega_2(p) := -\frac{U\rho_0(p)}{2} - \sqrt{\frac{U^2\rho_0^2(p)}{4} - U\rho_1(p)}. \tag{132}$$

The dressed self energy contribution is represented in Figure 21. A calculation in the same fashion as before starting from equation (109) and using the equations for the dressed quantities yields

$$\mathrm{Re}[\Sigma^\alpha(\omega,p)] = \frac{(1+N_f)}{N}\sum_k \int_{-\infty}^{\infty} dx A_k(x)\left[\frac{\omega}{\rho_0(p+k)}\right. \tag{133}$$

$$\left. -\frac{\rho_1(p+k)}{\rho_0^2(p+k)} + \frac{x}{\rho_0(p+k)}\right]\frac{1}{e^{\beta x}-1} + \mathcal{P}\int_{-\infty}^{\infty}\frac{\rho_{\Sigma,p}(x)}{\omega - x}dx \tag{134}$$

$$\mathrm{Im}[\Sigma^\alpha(\omega,p)] = -\pi\rho_{\Sigma,p}(\omega).$$

Assuming the sum rule holds, similar simplifications for the real part of the self energy exist like in the case of ρ_0. The spectral function of the self energy is given as

$$\rho^\alpha_{\Sigma,p}(y) = \frac{(1+N_f)}{N}\sum_l \int_{-\infty}^{\infty} dx \left(\frac{A_{l-p}(x-y)}{e^{\beta(x-y)}-1} f_p(x) - A_{l-p}(x-y)\frac{f_p(x)}{e^{\beta x}-1}\right). \tag{135}$$

This is again a convolution, but one where one function has a negative argument. This is obvious in the following alternative form.

$$\rho^\alpha_{\Sigma,p}(y) = \frac{(1+N_f)}{N}\sum_l \int_{-\infty}^{\infty} dx \left(\frac{A_{-(p-l)}(-(y-x))}{e^{-\beta(y-x)}-1} f_p(x) - A_{-(p-l)}(-(y-x))\frac{f_p(x)}{e^{\beta x}-1}\right) \tag{136}$$

Now we have expressed all necessary equations with respect to the full propagator. Using the Dyson equation given in (118), we now have a scheme for a selfconsistent fixed-point iteration.

5.5 Algorithm

In this section we will give a short overview on the main steps the calculation takes in practice. We will emphasize the structure of the equations previously given and restrict

ourselves to the selfconsistent calculation since it outperforms the non-selfconsistent method in speed and quality of the results. For a clear notation we drop flavor indices in this section.

The initial guess for the spectral function of the propagator is a Gauss-shaped peak at the position of the dispersion, since at zero temperature we would get delta-peak right at this position as in the boson case. The reason for this is that we have a non-degenerated ground state and a finite gap. The calculation of one iteration takes six major steps. We need to calculate the spectral function in the following order. We start with the calculation of ρ and then we turn over to f followed by ρ_Σ and the calculation of the zero and first moment of ρ to finally calculate the self energy. This could be used then to calculate A again. We introduce the symbol $*$ to denote a convolution that is performed with respect to momentum and frequency if the function also depends on that. Since the Bose function

$$n_B(x) = \frac{1}{e^{\beta x} - 1} \tag{137}$$

is often used we use the given short hand notation. We also introduce the operator S which acts as

$$S\rho_p(x) := \rho_{-p}(-x) \tag{138}$$

$$S\rho_0(p) := \rho_0(-p) \tag{139}$$

$$Sn_B(x) := n_B(-x) \tag{140}$$

and the operator of the principle value hilbert transform as

$$ph(\rho)(x) := \mathcal{P} \int_{-\infty}^{\infty} \frac{\rho_p(y)}{x - y} dy. \tag{141}$$

The first spectral function we need to calculate is ρ, which is given in this notation as

$$\rho = A * (A \cdot [n_B - Sn_B]). \tag{142}$$

The spectral function f now reads

$$f = \frac{-\rho}{ph(\rho)^2 + (\pi\rho)^2}. \tag{143}$$

We are now able to obtain the spectral representation of the self energy as

$$\rho_\Sigma = (1 + N_f) \left[f * (S[A \cdot n_B]) - (f \cdot n_B) * (SA) \right]. \tag{144}$$

We also need to calculate the zeroth and first moment of ρ by simple integration to express the self energy as

$$\mathrm{Re}[\Sigma(\omega, p)] = (1 + N_f) \left(\omega \left[n_k * \frac{1}{\rho_0} \right] - \left[n_k * \frac{\rho_1}{\rho_0^2} \right] + \left[n_{1,k} * \frac{1}{\rho_0} \right] \right) + ph(\rho_\Sigma) \tag{145}$$

$$\mathrm{Im}[\Sigma(\omega, p)] = -\pi \rho_{\Sigma,p}(\omega). \tag{146}$$

Here we have introduced the new shorthand

$$n_{1,k} = \int_{-\infty}^{\infty} \left(A_k(x) \frac{x}{e^{\beta x} - 1} \right) dx. \tag{147}$$

All in all we find that we need to implement, beside basic arithmetic operations, convolutions, integration and principle value hilbert transforms for an automated calculation. We refer the reader to chapter 6 for further information on the details of our implementation.

6 Computational Implementation

Since not all of the steps in the perturbation theory of the last chapter can be carried out analytically for arbitrary dispersion relations, we now build a numerical framework to deal with them. On the way we obtain a program which could be useful in a more general manner and works in one, two and three dimensions. In this chapter, we will go through the basic structure of the implementation in order to obtain a description of the asymmetry and broadening to be described in gapped hardcore bosonic models. The aim of our program is to calculate the spectral function of the propagator and related quantities. The calculation is performed on the computing cluster CL1 of the department of physics at TU Dortmund and is written in `C++` using the `C++11` standard.

This chapter is divided into 5 parts. The first section describes the design philosophy of the program. The next two outline the structure of the main two classes. The following section outlines some usage hints and the last describes how the calculations are performed in practice.

6.1 Design Philosophy

The key ingredients of our implementation are the following:

- Class Design
- Memory Efficiency
- Intrinsically Parallel Operations
- Discretisation
- Fast Convolution Algorithms

Class Design Considering the equations in section 5.5 that we need to implement, an object-oriented approach which represents be mathematical objects we deal with seems to be a good choice. If we take a look at for example Eq. (146), we notice what kind of mathematical objects exists beside plain numbers. We see two types of functions that we need to represent. One type is momentum dependent and the other depends on frequency and momentum. We will call these objects `kFunction` and `discreteDensity`, respectively. We sample functions on a mesh to represent them. The next question that arises is what kind of operations we need to perform with these objects, which will further restrict our possible design decisions. These include arithmetic operations, integration routines, convolutions of the two types and a Hilbert transform. Arithmetic operations that change the class type, such as the

multiplication of a `kFunction` with a frequency variable ω, yield a `discreteDensity` and is not dealt with in operator notation for clarity of notation.

Memory Efficiency Memory efficiency is an important issue since a spectral function in dimension two has a data tensor of rank three and since very sharp functions need to be resolved especially in frequency space. It is clear that at least this dimension needs many data points. Assuming we model a square lattice and taking a resolution of 128 points per dimension in k-space and 32768 points in frequency-space, we would make the `discreteDensity` more than 4.4 gigabytes in size. Therefore all arithmetic operations are performed on the object itself. The reason why there exists an operator `*=` but not `*` is, that this is the only practicable way to stick to the object-oriented approach without the need for unnecessary amounts of memory since in every operation a temporary object would be generated otherwise. All other functions make use of this 'in-place' philosophy as far as possible.

Intrinsically Parallel Operations The reason parallelization is used is the obvious advantage in speed. The execution time roughly halves when the number of threads running on individual cores doubles assuming that your problem becomes reasonable big in size as well. The object-oriented design makes it possible to make use of intrinsically parallel operations that don't need to be considered on the level of equation implementation. Operations on the objects are performed in a fashion that minimize the calculation of addresses in the tensor, exploiting the fact that some operands only depend on frequency or momentum in order to produce code that runs the best in parallel on the big data chunks. In general, all functions that perform operations on the often big data set are carried out in parallel with the help of OpenMP[38]. Since operations on the objects already happen in parallel, the user should not use these objects for own parallelization techniques. Otherwise the thread forking would stack up. Since these classes are intended to be mainly used, it is possible to avoid own parallelization and still benefit from multiple procession units. In the case of convolutions, that is done with the help of the FFTW3[39] unit methods.

Fast Convolution Algorithms Convolutions employ Fast Fourier Transform (FFT) routines, which make use of the circular convolution theorem and therefore force us to use a spatially uniform mesh in each variable of the function that was sampled. The principal value Hilbert transform is also carried out as a special kind of convolution using the Liu and Kosloff technique[40]. This means that instead of using this integral transform over frequencies we are using a faster and better suited approximation. It consists of making a convolution of the frequency dependence of the `discreteDensity` for every point in k-space with a suitable function that yields approximately the same result. In the limit of infinite sampling points and a compact support of the transformed function, this scheme would also be exact. We must also consider that the FFTW3 performs discrete Fourier transforms which are periodic. This is exactly what we want for the case of the k-space dependence if done right but wrong for the frequency dependence. To take this into account, we need to make use of the fact that a circular convolution is the same as a linear convolution if one half of the data points are zeros. The technique is called zero padding. This means, that be-

fore any convolution the half of both involved `discreteDensity`s in frequency-space has to be set to zero in a reasonable way. In the calculation we perform, the selected scheme for this procedure didn't have any significant influence on the results. The one we selected sets the continuous block of half data size to zero which has the least absolute integral weight. This scheme also intrinsically takes care of the fact that the integral convolution and the linear convolution are related by a shift in the sampled region up to a scaling factor. Therefore we don't need to adjust the padding scheme by hand for every convolution. Another important thing that one has to keep in mind is that a convolution performed in this way is still circular in the sense that data could be wrapped around from the highest to the lowest frequencies. This can be avoided by simply selecting a wide enough and well-positioned interval. Now consider the k-space sampling again: It has to fulfill the following properties to work as a fourier transform of our k-space sampling. We call A_i, $i = 1, 2, 3$, our set of primitive lattice vectors of the Brillouin zone and a_i will denote the vectors of the sampling mesh, so that a point p on the mesh takes the form

$$p = \sum_{i=1}^{3} n_i a_i, \tag{148}$$

where n_i are integer numbers. We want our vectors a_i to have at least the symmetry operations of the original lattice, which ensures that the periodicity of the FFT will be the same as the periodicity of the lattice and we need to be capable of writing the primitive lattice vectors as

$$A_j = \sum_{i=1}^{3} a_i N_{ij}, \quad N_{ij} \in \mathbb{Z}. \tag{149}$$

The last two constraints are that $N_{ij} = N_i \delta_{ij}$ must be diagonal for the FFT to perform correctly and that the mesh should be evenly distributed since we want to approximate the thermodynamic limit. To find an optimal pair of those vectors that fulfill the desired conditions and have an optimal resolution with respect to memory consumption could be a hard task if the lattice symmetry is complex. For further information on this topic, see [41].

6.2 The kFunction Class

In this section we will go through the interface of the class `kFunction`, which will represent all functions that only depends on momentum. We begin with the creation of an instance of the class.

Constructors/Assignment Operators The constructors and copy/move constructors/assignment operators present are

```
kFunction(unsigned int m_dimensionality,double *data,
    const ptrdiff_t* kPeriodicity,const double *k_low,
    const double *k_high);
kFunction(const kFunction& copy_from_me);
kFunction(kFunction&& copy_from_me);.
```

```
kFunction& operator=(const kFunction& Arg_kFunction);
kFunction& operator=(kFunction&& Arg_kFunction);
```

If the `kFunction` is not created by integrating a `discreteDensity`, it can be copied or moved from an already existing `kFunction` or created by handing over the initial data in the form specified in section 6.4. The last option usually happens in the beginning of the calculation when we bring the dispersion in the compatible format. In the case of the dispersion it is just sampled with a mesh as described above to bring it into a uniform format. To do so one has to use the row major format with the last dimension padded as noted in the FFTW3 manual [39] for in-place transforms, which is again done to reduce the memory requirements. Since a move constructor and assignment operator is provided, the performance of dynamical objects is the same as of stack objects. But dynamical objects make resource management easier.

Arithmetic Operations Next we list all operations that we want to apply to `kFunction`s.

```
kFunction& operator-=(const kFunction& Arg_kFunction);
kFunction& operator+=(const kFunction& Arg_kFunction);
kFunction& operator*=(const kFunction& Arg_kFunction);
kFunction& operator*=(double x);
kFunction& operator-=(double x);
discreteDensity multiply_by_x(ptrdiff_t xLength, double x_low,
    double x_high);
kFunction& square_kFunction();
kFunction& invert_kFunction();
```

The operators in operator notation are just used as the equally named ones for double values. Operations are carried out pointwise and in parallel. The righthand operand could then be a `kFunction` or a simple `double` factor. The function `multiply_by_x()` multiplies the `kFunction` by a frequency variable in the range given in the argument and with the resolution specified through `xLength`, which yields a `discreteDensity` object. This variable has to fit to the other used `discreteDensity` objects in a given calculation to yield reasonable results. The functions `square_kFunction()` and `invert_kFunction()` calculate the square of the `kFunction` ρ_k as ρ_k^2 , as well as $1/\rho_k$ in place.

Convolution

```
kFunction& convolution( kFunction& Arg_kFunction,
    bool keep_arg_unchanged);
```

This function calculates the cyclic convolution with `Arg_kFunction` and stores it in the initial `kFunction`. `Arg_kFunction` is kept unchanged if the last flag is set to `true`, otherwise it becomes useless after the operation. On the other hand setting the flag to false safes calculation time.

Data Access

```
const double* get_data_read_access() const;
```

This function returns a readable pointer to the data chunk, which is kept in row major format with the last dimension padded. For further information see the usage hints section. There also exists a header which calculates the logical address, called `row_major_order_access.h` and containing the function

```
ptrdiff_t  row_major_order_access(int rank,
    const ptrdiff_t *dimensions,ptrdiff_t k, ... ).
```

Here, rank has to be the rank of the tensor, that is the dimension+1. The following argument contains the tensor layout and the next arguments contain the index at each dimension whose address should be calculated.

6.3 The discreteDensity Class

In this section we will discuss the class `discreteDensity`, which will represent all spectral functions of the theoretical calculation of the Brückner approach. For this, we go through the layout of the class and discuss how it can be used. We again start with the construction of an object.

Constructors/Assignment operators The constructors and copy/move constructors/assignment operators defined for `discreteDensity` are

```
discreteDensity();
discreteDensity(unsigned int dimensionality, bool initialize,
    const ptrdiff_t* x_kMeshsize, double x_low,double x_high,
    const double* k_low,const double*  k_high);
discreteDensity(unsigned int dimensionality, double* data,
    const ptrdiff_t* x_kMeshsize, double x_low,double x_high,
    const double* k_low, const double*  k_high);
discreteDensity(const discreteDensity& copy_from_me);
discreteDensity(discreteDensity&& copy_from_me);
discreteDensity& operator=(const discreteDensity& argDensity);
discreteDensity& operator=(discreteDensity&& argDensity);.
```

Similarly to the previous case, a `discreteDensity` could be copied or moved from an already existing `discreteDensity` or created by handing over the initial data. Otherwise it could be created by calling the function `multiply_by_x()` on a `kFunction`. Handing over the initial data is typically used to set up the initial guess for the density as it is described in section 6.5. The array format has to be a row major format, with the last dimensin padded as described in the section on usage hints. Again, a move constructor and assignment opertor provides the same performance for dynamical objects as with stack objects.

Arithmetic Operations Listing all needed arithmetic operation to implement the Brückner-approach leads to the following operators:

```
// operators related to densities
discreteDensity& operator-=(const discreteDensity& argDensity);
discreteDensity& operator+=(const discreteDensity& argDensity);
discreteDensity& operator*=(const discreteDensity& argDensity);
discreteDensity& operator/=(const discreteDensity& argDensity);
discreteDensity& square_density();

// operators related to scalars
discreteDensity& operator*=(double Arg_Scalar);

// operators related to xFunctions
discreteDensity& operator*=(double (*x_Arg_Function)(double));
discreteDensity& operator+=(double (*x_Arg_Function)(double));

// operators related to kFunctions
discreteDensity& operator*=(const kFunction& Arg_kFunction);
discreteDensity& operator+=(const kFunction& Arg_kFunction);
discreteDensity& operator-=(const kFunction& Arg_kFunction);.
```

An xFunctions is a function that depends on frequencies only. It has no special class because it would introduce unnecessary overhead. Instead regular functions having one double valued argument and return a double value are used to describe those. These operator's usage is largely self-explanatory.

Convolution

```
discreteDensity& convolution(discreteDensity &Arg_Density,
    bool keep_arg_unchanged);
discreteDensity& negative_convolution(discreteDensity &Arg_Density,
    bool keep_arg_unchanged);
```

In our calculation scheme we come across those two types of convolutions. Both the regular and negative convolutions are taken with respect to frequency and momentum. Since these convolutions are carried out using fast convolution algorithms which relay on FFTs we need to be aware of errors introduced which come along with this approximation. Further details could be found in section 6.1. The result is always saved in the `discreteDensity` you call from. As before, you can keep the other argument `discreteDensity` intact but sacrifice performance by setting `keep_arg_unchanged` to true. The function `negative_convolution()` should be interpreted as taking a regular convolution with the argument `discreteDensity` used with a minus sign in front of its momentum and frequency argument as in (144).

The Principal Value Hilbert Transform

```
discreteDensity& principalValueHilberttransform();
```

This function calculates the principal value Hilbert transform of the parent object in place.

Data Access In this paragraph, we give a short summary on how to access the data directly when needed.

- `double* get_data_read_access()` works as described in the section on `kFunction`s.
- `ptrdiff_t* get_Meshsize()` returns a pointer to array containing the sampling rates along all dimensions. You can access it with `[]`. In 2D the resulting output would be an array of size three starting with the frequency dimension.
- `double get_x_low()` returns the lower frequency bound.
- `double get_x_high()` returns the upper frequency bound.
- `double Element(ptrdiff_t k=0,ptrdiff_t l=0,ptrdiff_t m=0,ptrdiff_t n=0)` gives access to the element in the tensor at the given index (k,l,m)

The header `row_major_order_access.h`, as mentioned in the `kFunction` section, could be used as well.

Integration

```
kFunction xIntegrationWeighted(double (*x_Arg_Function)(double)) const;
kFunction Integration() const;
```

Here xFunctions represent a function with a single frequency dependence as before. These integration routines integrate the frequency part of the `discreteDensity` and yield a `kFunction`. In the case of the `xIntegrationWeighted()` the function in the argument will be multiplied and the result integrated.

Serialization This class is capable of being serialized with BOOST serialization methods[42]. This is particularly useful since it takes a lot of time to calculate a spectral function and it may be necessary to continue working with it. To this end, it is possible to store it to disc and load it again later on. Below, an example for saving and loading this object is given.

```
// create and open a character archive for output
std::ofstream ofs("rho.obj");
// save data to archive
{
boost::archive::text_oarchive oa(ofs);
// write class instance to archive
oa << *tmp_d1;
// archive and stream closed when destructors are called
 }

// ... some time later restore the class instance to its orginal state
```

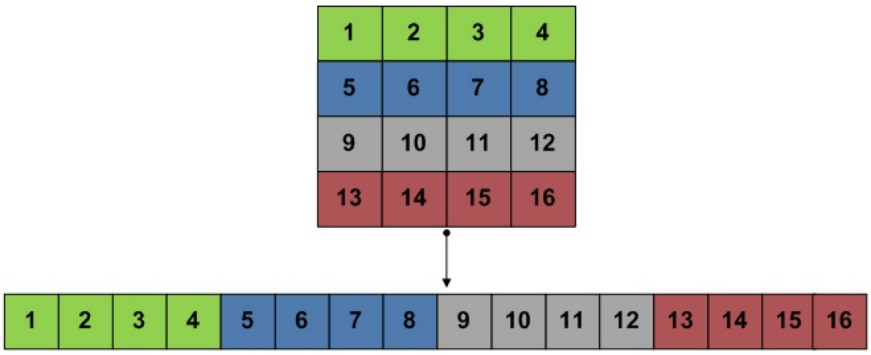

FIG. 22. Row major format in the case of two dimensions. Lower part represents the memory layout of the upper matrix. Taken from Ref.[43].


```
delete tmp_d1;
tmp_d1=nullptr;
tmp_d1=new discreteDensity();
{
// create and open an archive for input
std::ifstream ifs("rho.obj");
boost::archive::text_iarchive ia(ifs);
// read class state from archive
ia >> *tmp_d1;
// archive and stream closed when destructors are called
}
```

6.4 Hints for Usage

In this section we will give you some advice to keep in mind when using the provided code. Among these is information about the internal structure of the data, performance, numerical stability concerns, parallelization, useful headers and files as well as cleanup of remaining allocated memory after execution. The last paragraph lists all libraries the program relies on.

Format of the Double Data Block While the usage of the FFTW3 routines forces us to use their format, we decided to consistently stick to it since it has a good performance and the smallest possible memory footprint. It is important to mention that we use the in-place format that is special from the out-of-place format. The format we use is the so-called row major format with the last dimension padded. That means that the index of the last rank of the tensor varies the quickest, see Figure 22. The padding has to be understood in the following manner: Assuming we decide to create a sampling mesh of the dimensions n_i with $i \in \{0,..,d\}$ where d is the k-space dimension. In that case we need to create a row major format data array of the dimensionality $n_1, \ldots 2\cdot(\lfloor n_d/2 \rfloor + 1)$. Than we use the addresses as they are in created object and leave the ones with the last index bigger than d undefined. They are for internal purpose only. Memory needs to be allocated using the method `fftw_malloc()`

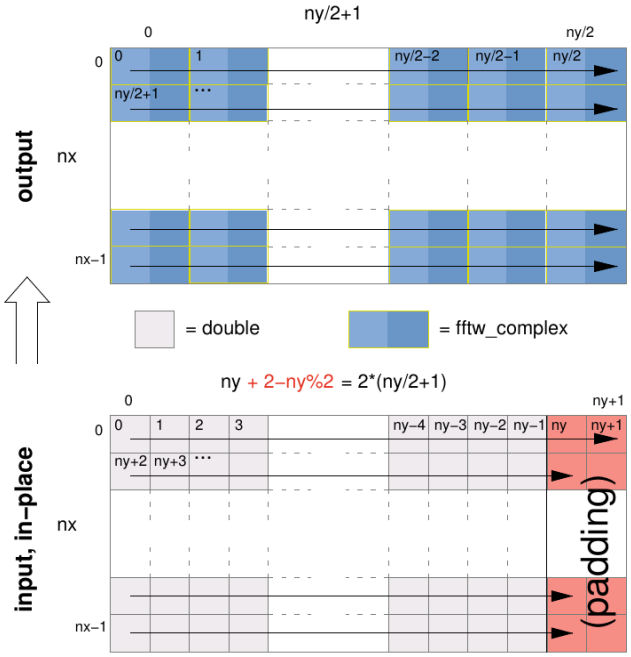

FIG. 23. In-place format with padding in the case of two dimensions. The lower matrix depict input structure and the upper matrix represent the output format of a FFT. Taken from Ref.[39].
Copyright FFTW©

instead of `new` or `malloc()`. Once this data chunk is handed over to the constructor of either objects it takes care of destroying them. This means that memory cells which have a last index bigger than d carry no data needed on the outside of the object. The last one or two memory cells in this dimension have no meaning to the tensor before the FFT is applied, see Figure 23. For the user not interested in anything else but the complete convolution, the interpretation of the output format of the FFTW3 is of no importance. For further details refer to the manual [39]. Since the FFTW3 is used it is necessary to allocate the memory used for all object by a call to `fftw_malloc()` . The last point to mention here is that it is important to choose the first index to refer to the frequencies. This arbitrary choice was made to keep calculation simpler in the majority of of cases, but the internal interpretation of the object relies on it.

Performance Optimization For the optimal performance of this method, the same considerations have to be taken into account as for usual double arithmetic: That means keeping the count of needed operations as low as possible since all implemented arithmetic operations on the object need an execution time that scales linearly with the size of the object. Additionally, copying an object at the right time can save calculation time. For example: When operations have to be applied to multiple copies of one object it works faster to make one copy, apply the operation and then copy from the final object. For optimization it often makes sense to write two files of code. One where it is easy to follow the meaning of objects as a unit test and another which is optimized with respect to memory and calculation time consumption to compare the results of each in order to trace back errors. Another influence on the performance is

given by the tensor layout. The reason for this is the use of FFTW3 routines. For the size and dimensions of the data array, there are currently no limitations other than the accessible amount of memory on our machine, but since FFTs are used, the classes perform best with sampling rates of each dimension composed of small prime numbers. Especially powers of two are recommended wherever possible.

Numerical Stability Numerical stability is an important issue in dealing with iteration schemes like this. It is often useful to trace back this issue by plotting results and taking a look at how they behave when certain cut-offs are applied. In the case of the Brückner-Approach used in this thesis, functions with a frequency dependence have to be multiplied to the `discreteDensity` that had a pole at zero. This needed to be cut off by setting the function value close to zero which does not matter nevertheless since we know that the `discreteDensity` as spectral function has to be zero as well. It often is not precisely zero due to numerical fluctuations. Divisions have been cut off in the order of magnitude of the numerical fluctuations as well. And as the last point to mention, left over wraparound effects of the FFT used in convolutions can sum up on iterations. This can be avoided in our case by setting the sampled interval reasonably large. To trace these effects it is usually a good idea to investigate the behavior of a convolution over a few iterations.

Parallelization In order to use the parallelization provided by the classes, it is necessary to initialize OpenMP[38]. Therefore the header `omp.h` needs to be included and the following lines should be added at the the beginning of your main method:

```
omp_set_num_threads(n_cores);
std::cout << "Running with "<<omp_get_max_threads()<<" threads!"
  << std::endl;
if(!fftw_init_threads())
   std::cerr << "Failed to initialize parallelization" << std::endl;
else
   fftw_plan_with_nthreads(omp_get_max_threads());
```

Here, `n_cores` is an int-type and has to be set to the number of threads you want to use. This is usually the number of available cores of the system.

Useful Headers and Files Beside the outlined classes there exist a few other files we want to mention here. Some of them just contain helper functions for the actual classes, while others have a more general purpose.

The headers that are necessary for the classes to operate are `invert_dataArray.h` and `zeropadding_optimizer.h`. `invert_dataArray.h` is used to transform a `discrete Density` to a version with the opposite sign in all arguments. `zeropadding_optimizer.h` is a padding routine which selects the best padding interval on its own by measuring the absolute weight. It would be possible to select the padding scheme by hand as well, but since it showed no difference it was kept in this state for comfort and because it makes it easier to notice wraparound errors. The header `padding_transform.h` which contains a routine that transforms the padding scheme in-place, is not in use anymore. This is due to its major negative impact on the runtime, but it was kept because it

could be used two further reduce the memory consumption at the downside of longer operation time. If an extension to run in full parallel becomes feasible, it might be a good option to consider, when memory becomes an issue. The padding transformation is needed because the hilbert transform and regular convolutions depend on different Fourier transforms. The previous version is commented out but still in place. Some other headers exists two make it easier to work with the uncomfortable row major order format. These are `row_major_order_access.h` and `stride_pointer.h`. The first one contains a function

```
ptrdiff_t  row_major_order_access(int rank,
 const ptrdiff_t *dimensions,ptrdiff_t k, ... )
```

as described in the section on `kFunction`s in the paragraph on data read access. It makes it possible to get an address from an index for a padded row major format as used by FFTW3. For further detail refer to this section. `stride_pointer.h` is a header that provides a random access iterator that behaves like a pointer with a step width of a multiple of the data type it refers to. It could be used to iterate through every frequency point for one k-space point. It is designed as a template and works for all data types. The last headers to mention are `calc_iteration_step[_multiflavour].h`, which could be called to calculate a step in the Brückner approach calculation. This is described more precisely in the next section. Beside that, there also exists an unit test for both classes named `test.cpp` that should be extended to continue the unit test driven development. It could be used to test and debug the program. Any upcoming errors should be added here as a test case if possible. It is based on the framework UnitTest++[44].

Libraries and Requirements The code provided here should be compiled with a `C++11`- and OpenMP[38]-compatible compiler. The libraries required for compilation are:

- boost[42]
- FFTW3[39]
- UnitTest++[44]
- OpenMP[38]

UnitTest++ is required just for testing.

Cleanup At the end of the calculation make a call to the function

```
fftw_cleanup()
```

to free all memory acquired by the FFTW3 routines since it is called from within the two classes. This is needed to free all resources that were not allocated explicitly, since FFTW3 saves acquired knowledge of efficient calculation to speed up the process of finding such routines in later runs.

6.5 Calculation of the Propagator Spectral Function

In this section we describe how our code can be used to calculate the propagator spectral function and all the other quantities that could be derived from it. The usual use case is divided into four steps. In pseudo code notation, these steps are

```
initialization()
begin loop over temperatures
    begin loop over Brückner approach calculation steps until convergence
        mean field update if required
    end
    calculate quantities of interest
end
```

The initial guess for the spectral function of the propagator is a Gauss-shaped peak at the position of the dispersion, since at zero temperature we would get a delta-peak right at this position as in the boson case. The reason for this is that we have a non-degenerated ground state and a finite gap (one particle does not know its statistic).

Initialization Firstly we set the initial guess of the spectral function to a gaussian peak at the position of the dispersion relation as discussed in section 5.5. Secondly, we need to initialize the dispersion with a mesh that fulfills the requirements mentioned in the paragraph on fast convolution algorithms to bring it into a uniform format. Naturally, both need to be described with the same mesh in k-space. Due to our class design it is important the frequency is associated with the first index. For the format of the sampled input it is necessary to stick to what was outlined in the paragraph on the Format of the Double Data Block.

Loops Once the initial data-sets are created, we can start to define a loop over temperatures for which we want to calculate the quantities we are interested in. In this loop we need a inner loop that iterates the Brückner approach steps until the selfconsistent calculation reaches a stationary state. If we also apply a mean-field-approximation for an additional interaction we need to calculate the new dispersion from the new propagator guess in each iteration step and create a mixing update for stability reasons. That means that we average over the old dispersion relation and the retrieved one. How this is done from the theoretical perspective is described in chapter 3. In practice, it was done by a direct access to values of the `kFunction` $n_k = \left\langle b_k^\dagger b_k \right\rangle = \int_{-\infty}^{\infty} A(k,x) n_B(x) dx$ ($n_B(x)$ denotes the Bose function) since it is easier to calculate in complex numbers and the k-space resolution was low enough that the calculation speed was no real problem. After convergence is reached, we are safe to calculate results and start over with next temperature value. As a measure for convergence the last three particle numbers $n(T) := \frac{1}{N} \sum_k < b_k^\dagger b_k >$ were used by taking the relative error to their average for two pairs.

Brückner Approach Iteration Step The calculation of the self-consistent Brückner approach steps should be performed using the methods that are defined in the header `calc_iteration_step[_multiflavour].h`. The part in the braces should be

omitted in the single flavour case and has to be used in the triplon case. If we want to use it we need to pass the needed information to this interface, which has the following signature:

```
calc_iteration_step(kFunction *dispersion_disc, discreteDensity *&A,
    double arg_beta, bool energy_output, bool A_output).
```

The first argument is the spectral function of the propagator, the second the dispersion relation and the third, `arg_beta`, is the inverse temperature. The last two flags trigger an output method for the `discreteDensity` after this iteration step and for the real and imaginary part of the self energy. All this output is just given for the k-space point $k = 0$. We recommend to use this function since it is designed to work with the least amount of memory and computation. One the other hand it makes it hard to recognize the equation given in the chapter of the theoretical description. This should be kept in mind if working on this file or creating a custom calculation scheme from it. Since this file has simple output capabilities for a minimal script, no own output functions are needed. For details on the output format refer to the header source.

7 Numerical Studies of the Spectral Density in 2d

In this chapter we will numerically investigate the properties of the spectral function of the propagator as described by the Brückner approach. As described in chapter 2, we want to understand effects from non-trivial scattering processes in hardcore bosonic models: The asymmetric curve shape of the propagators spectral function, the band narrowing with increasing temperature and the broadening of the peaks associated with particle states. We discuss these effects in the context of the effective models for VOPO and Cs_2CuCl_4 as well as a toy model proposed to pin down effects that are related to the change of the dimensionality.

For one-dimensional systems the existences of the hardcore bosonic effects was already confirmed by Fauseweh et al. [8, 7] and for Cs_2CuCl_4 in two dimensions but with a focus on other effects, by Simon et al. [21]. These results provide an additional check for the consistency of our calculations. For the one-dimensional case we retrieved and verified the same results, but since our focus lies on 2D-systems these are not presented here.

The momentum space will be described in the following form: VOPO and the toy model are parameterized with regular Cartesian coordinates and for Cs_2CuCl_4 we use the the vectors given in chapter 3. All plots are generated using 128 points for each momentum space direction and 131072 points for the frequency space. In the case of VOPO, one momentum space direction is sampled with twice this resolution to form a uniform mesh. For the sampling of the temperature axis 6 points were used since they have a strong influence on the computation time.

We will start with the discussion of the VOPO and Cs_2CuCl_4 crystals without mean-field interaction and will keep our discussion minimal by giving one example for both crystals, where the findings will apply to both systems. Then we will outline how the mean-field interaction renormalize the dispersion relation. Finally, we will take a closer look on the effects of dimensionality with the help of our toy model.

7.1 Observations on VOPO and Cs_2CuCl_4

This section will present our findings for of VOPO and Cs_2CuCl_4 as representatives of more general hardcore bosonic models. Since our results are obtained with the Brückner approach, their plausibility reflects back on the validity of its assumptions.

General Shape of the Spectral Density In all calculations curve shapes exhibited the form represented in Figure 24 throughout the considered temperature regions. We take VOPO as an example but obtain similar plot for Cs_2CuCl_4. It shows asymmetry with the tail oriented to be middle of the band, broadening and peak position shift with

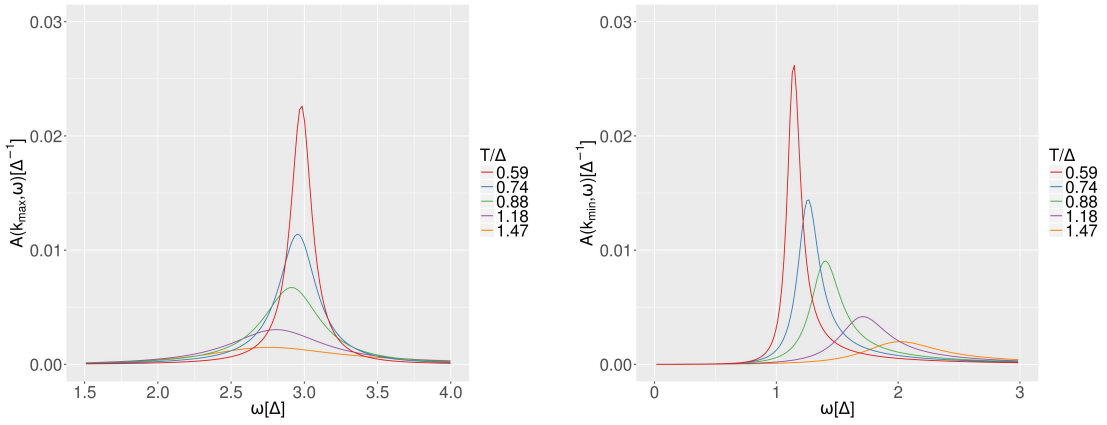

(a) Maximum mode (b) Gap mode

FIG. 24. Line shape of the gap and maximum mode of the crystal VOPO

increasing temperature which is the behavior that we associated with these gapped hardcore bosonic models. Since the general shape stays the same in all cases we further investigate the behavior of these models using a set of different parameters that are related to this curve shape.

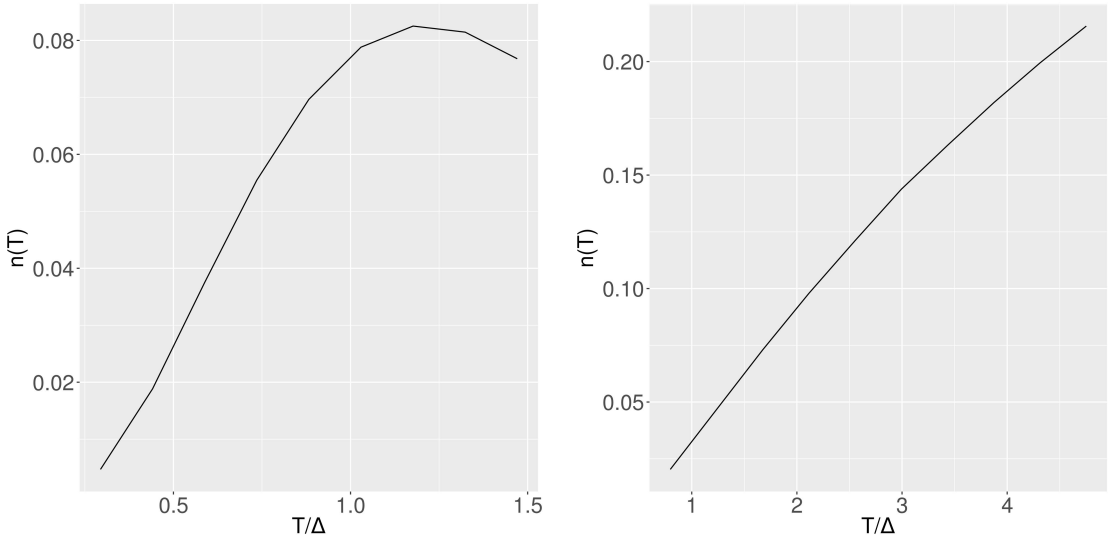

(a) VOPO (b) Cs_2CuCl_4

FIG. 25. Temperature dependence of the particle number of VOPO and Cs_2CuCl_4

Particle Number The particle number can be obtained for the spectral function of the propagator using equation (128). In the case of 1D systems, where a benchmark against an analytically solvable spin chain with next neighbor hopping exists, the particle number seems to be preserved by the self consistent approximation in the

single flavour case[7] up to numerical accuracy. However, in the multiflavor case the approximation showed unphysical behavior since it is not monotonic and a drop in the population of particles with increasing temperature doesn't make sense. This effect was observed in one dimension in Ref.[8], but the reasons behind this are still unclear. Our calculations for VOPO which are displayed Figure 25 exhibit the same unphysical behavior, showing that it is also present in higher dimension. On the other hand the particle number curve of Cs_2CuCl_4 seems plausible, which is consistent with the hypothesis that the effect only appear in multiflavor systems like VOPO.

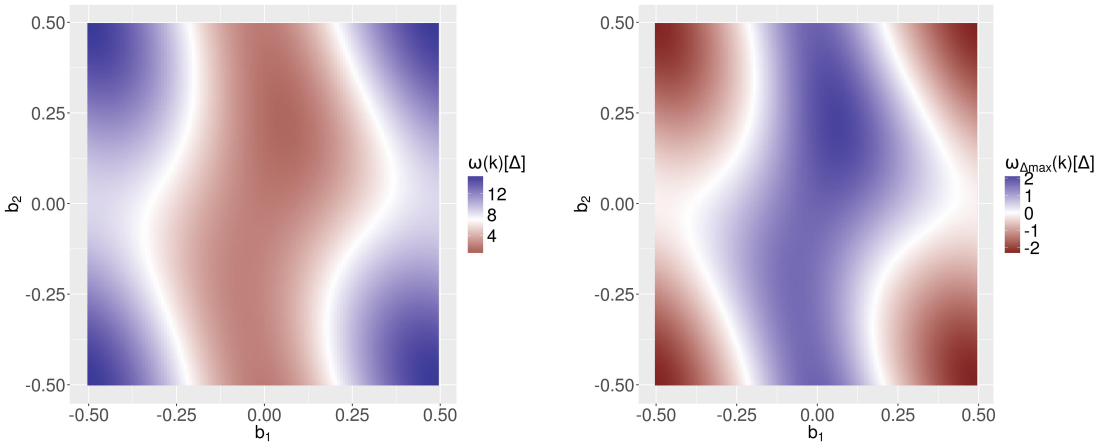

(a) Cs_2CuCl_4 dispersion (b) Cs_2CuCl_4 relative peak shift

FIG. 26. Dispersion relation of Cs_2CuCl_4 and relative shift of the peak position at $T = 4$ K relative to the dispersion relation which is also the peak position at zero temperature

Peak Shift and Band Narrowing Since $A(k, \omega)$ is given at zero temperature as a δ-peak located at the band energy it is reasonable to compare the shift in position relative to the dispersion as $\omega_{\Delta max}(k) = \omega_{max}(k) - \omega(k)$, where $\omega_{max}(k)$ is given by the frequency of the maximum of the spectral function $A(k, \omega)$. This quantity is depicted in Figure 26. We see that low-lying regions have a positive shift in the energy and high-lying a negative shift leading to a narrowing of the band. The shift nevertheless is not equally pronounced for higher and lower lying modes. This is clear from Figure 27, which shows the shift of the highest and lowest mode with temperature: The lower lying modes have a more pronounced upwards shift than the high modes move downwards. Since the rising density of hardcore bosons at higher temperatures blocks free propagation, states with low-lying energy are favored.

Asymmetry We now take a closer look at asymmetry of the curves. Figures 29(b) and 30(b) depict the asymmetry described as $\omega_{\text{asym}}(k) = \omega_{max}(k) - a(k)$, where a represents the middle of both points around the maximum that have half height on the curve as depicted in figure 28. In the first regime up to 0.8 Δ we notice that tails point to the middle of the band as expected. Again the tendency for a stronger tail at the low end of the band is visible. This could also be explained as an asymmetry in the accumulation of particles towards in low-lying states. In the case of VOPO

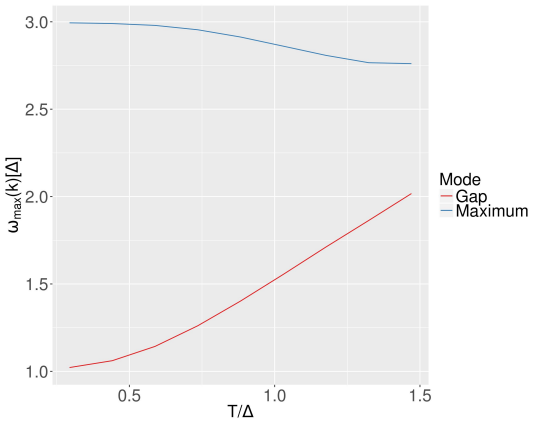

FIG. 27. Absolute peak position of gap and maximum mode of VOPO

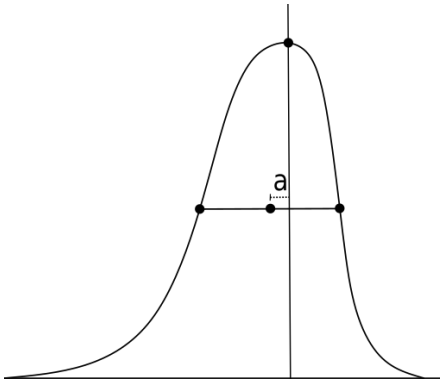

FIG. 28. Measure of asymmetry

the tail direction of the high energetic states changes and point upwards as well at elevated temperatures. Since no obvious reason exists for this and the particle number becomes unphysical around the same temperature, we interpret this as a break down of the Brückner approximation.

Broadening Broadening effects are depicted in Figure 29(a) and 30(a). We use the full width at half maximum for measuring the width. The figures show that higher modes tend to show stronger broadening. This seems reasonable since the width is related to the lifetime of particles. The overall exponentially-shaped increase with temperature is also expected since scattering between the rising number of particles should become more and more important.

Mean Field Approximation Effects As we discussed in chapter 3, mean-field interactions lead to a renormalization of the dispersion relation. To compare the effect of the additional terms we subtracted the dispersion relation from the renormalized dispersion relation to make effects visible that are purely related to the additional interaction. As we can see from Figure 31, we have an overall shift in the energy leading to an increase of the effective gap. This leads to a range of applicability of

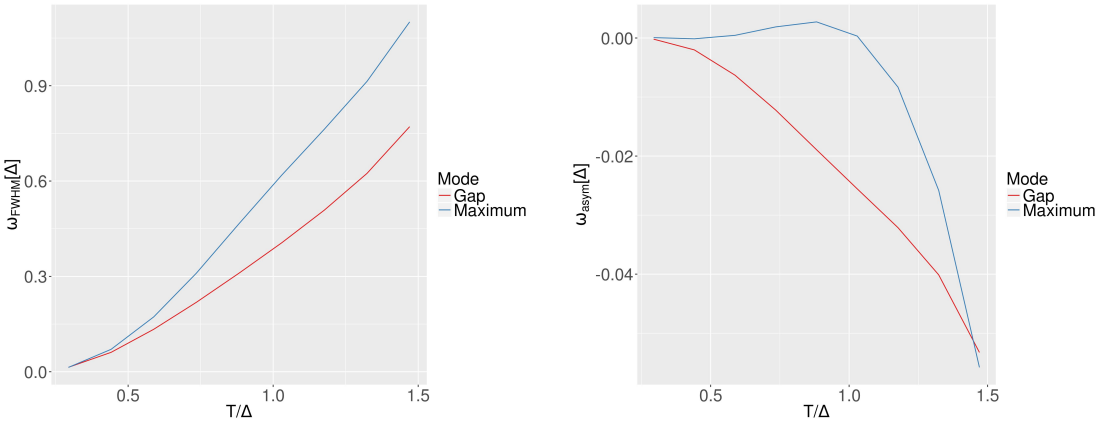

(a) FWHM (b) Asymmetry

FIG. 29. Temperature dependence of the asymmetry and FWHM of VOPO

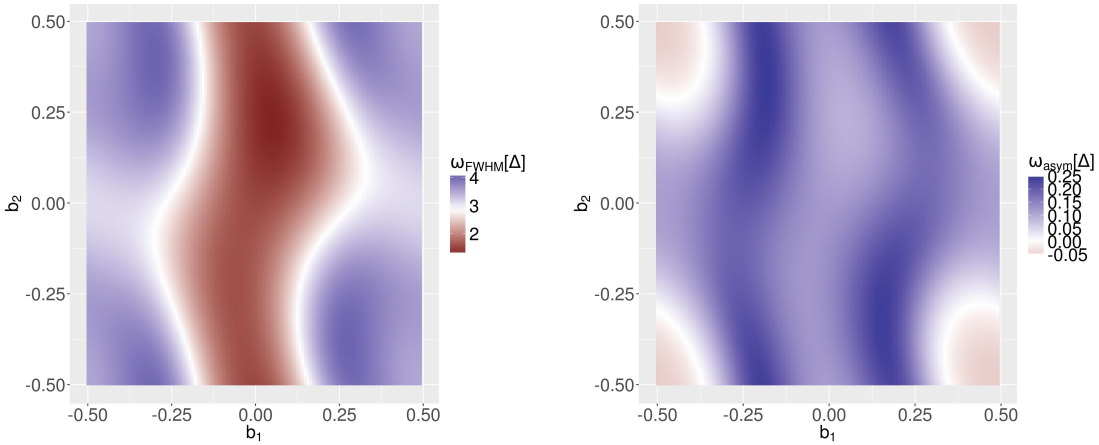

(a) FWHM (b) Asymmetry

FIG. 30. Asymmetry and FWHM of Cs_2CuCl_4 at $T = 4$ K

the theory up to higher temperatures since our perturbative suppression is related to this gap energy. Beside the overall shift we also notice that lower energies are shifted stronger than higher-lying modes, leading to a additional narrowing of the band.

7.2 Observations on a Toy Model

Our toy model Hamiltonian is given as

$$H_\lambda = \sum_{\mathbf{k}} \left(\Delta + \frac{W}{2(\lambda+1)} (1 + \lambda - \cos(k_x) - \lambda \cos(k_y)) \right) b^\dagger_{\mathbf{k}} b_{\mathbf{k}}. \tag{150}$$

For $\lambda = 0$ we have a completely decoupled effective 1D system, whereas for $\lambda = 1$ the system is homogeneously coupled in both directions and behaves two-dimensional. In

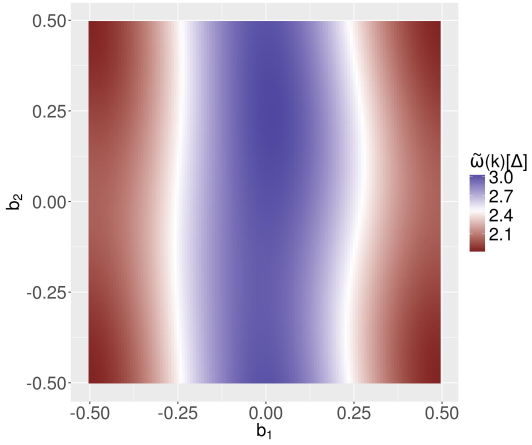

FIG. 31. Difference of the dispersion and the renormalized mean-field dispersion for Cs_2CuCl_4 at $T = 4$ K

the case of $\lambda = 0$ we replicate the results from Ref. [7] for the cosine band as expected. We keep the parameter $\Delta = 1$ fixed and consider two different values for the bandwidth W, $W = 0.5\Delta$ and $W = 4\Delta$. Since the plots don't differ significantly we only present the behavior at the band gap. We select this **k**-point since it is stationary with respect to λ. Since the only observation that strongly depends on the band width is the particle number, we will omit plots for the wide band. The line shape of the spectral function are not given since all observed line shapes look rather similar as the previously given ones.

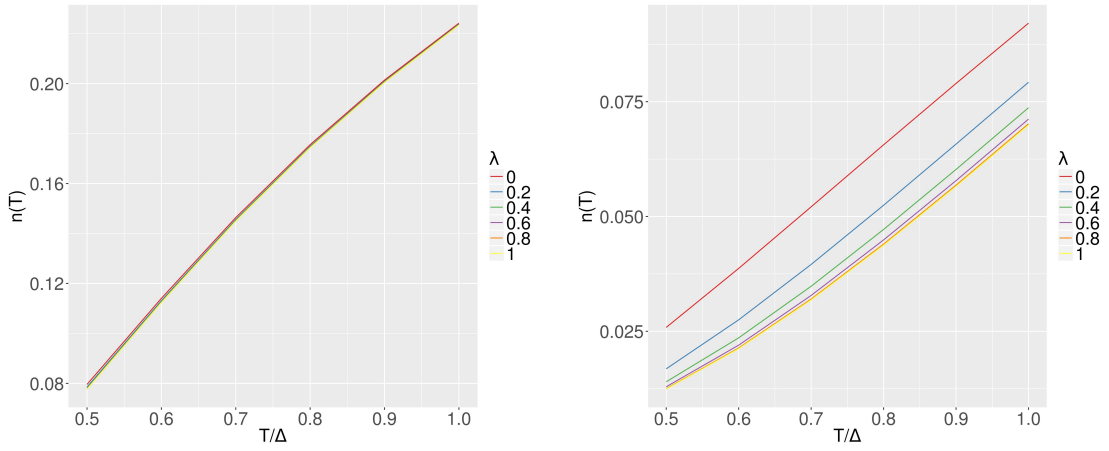

(a) $W = 0.5\Delta$ (b) $W = 4\Delta$

FIG. 32. Temperature dependence of the particle number of the $W = 0.5\Delta$ and $W = 4\Delta$ bandwidth toy model

Particle Number When we take a look at the particle number of the toy model for different band types in Figure 32, we observe two quite distinct behaviors for both

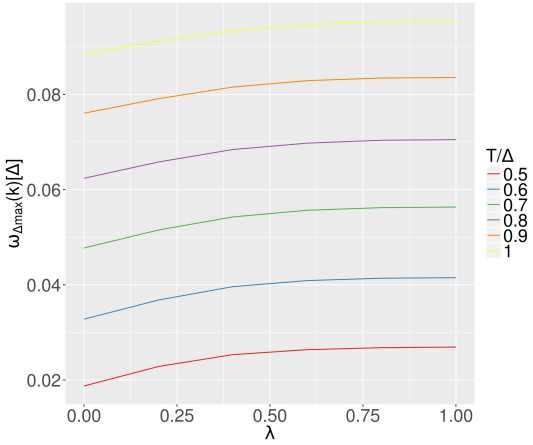

FIG. 33. λ dependence of the peak shift of the $W = 0.5\Delta$ toy model

bands. In the case of the small band the additional coupling has just only a small effect on the particle number whereas for a wide band there is a drastic decrease in the number of particles. Fauseweh et al. [8] hypothesize that for a band with fixed bandwidth and gap energy the particle number of the 2D model should roughly scale with the square of the particle number of the 1D model with the same parameters. The argument relies on the fact that the additional space at low frequencies that avoids a pile up should grow quadratically. This argument seems to fail in the flat band case. On the other hand for low temperature regime of the wide band this argument might hold. The gradual decline of the particle number with increasing coupling strength could be understood in terms of particle states laying at low band edges being related to the inverse of the gradient of the band, as known from the discussion of van Hove singularities, and therefore additional curvature leads to fewer particle states.

Band Narrowing Taking a look at the peak shift as given in Figure 33, we get a different effect regarding the influence of the dimensionality on the bands than in the case of particle numbers. Here for both bands the peak shifts become stronger with increasing coupling constants. The reason for this remains unclear.

Asymmetry Considering Figure 34, we find the opposite observations as in the case of the peak shift. For both bands the the additional coupling make the curve shape more symmetric. This is consistent with the hypothesis that particles pile up less, leading to less asymmetry yielded by complex scattering processes.

Broadening We notice that for the same reasons the width of the peak becomes sharper with increasing coupling strength which is related to less coherence loss by particle scattering.

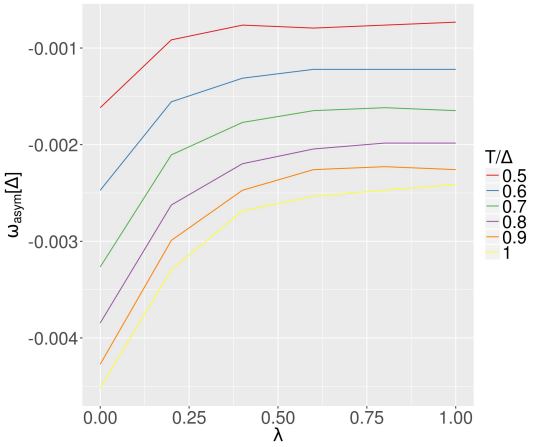

FIG. 34. λ dependence of the asymmetry of the $W = 0.5\Delta$ toy model

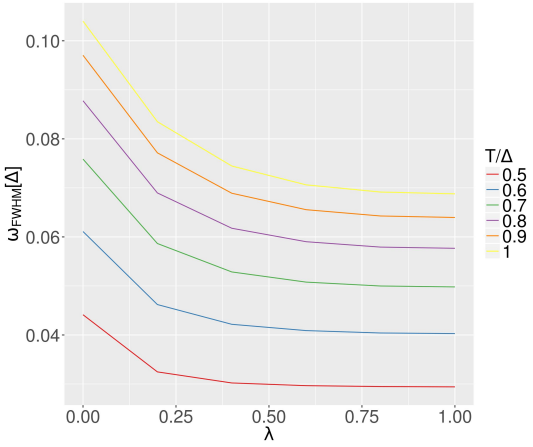

FIG. 35. λ dependence of the FWHM of the $W = 0.5\Delta$ toy model

8 Summary

The appeal of the perturbative Brückner approach we presented is its independence of dimension and its extensibility to include additional interactions or possibly higher orders of the perturbation series. It has proven to work well in one dimension where it could be benchmarked against simple next-neighbor hopping models. Its one-dimensional self-consistent extension even seems to retain the sum rule at finite temperatures in the single flavour case up to numerical accuracy.

In general all observations on the lines shapes asymmetry, broadening and shift of the peak position from 1D models could be confirmed to extend into higher dimensions. That also includes the unphysical behavior of multiflavour systems in higher dimensions. We considered for this as candidates for a hardcore bosonic description the VOPO and Cs_2CuCl_4 crystals. Observations on a toy model confirmed that the influence of the additional space that particles can propagate into decreases the pile up of excitations and therefore leads to a decrease in broadening and asymmetry, but also suggested a more complex dependence of the particle number. Since scattering processes seem to decrease, one could expect the expansion to perform better in higher dimensions. Clearly our numerical studies could not pin down exact relations. We developed a flexible code framework for this and similar calculations that can handle high memory loads for high resolutions. This framework might also be considered as a starting point for future development of this method. Further we noticed that the a posteriori assumption that the sum rule is conserved leads to further simplifications in the equations of the selfconsistent approach. This idea might be used to obtain new insights on the equations itself.

In future work, it would be interesting to find exact reasons for the observed behavior. It would also be possible to include additional interactions as performed in 1D to study its influence on the dimensionality or take into account higher perturbation orders.

Acknowledgements

I indebted to Prof. Götz Uhrig and Benedikt Fauseweh for providing a very interesting topic and always extending a helping hand.

I also want to thank my friends Aaron Gootjes-Dreesbach, Hannah Skibowski and Stephan Escher for support and comments on the draft, as well as my parents Dieter and Waltraud for all that owe I to them.

References

[1] Christian Knetter and Goetz S. Uhrig. "Perturbation Theory by Flow Equations: Dimerized and Frustrated S=1/2 Chain" (June 2000), Eur. Phys. J. B vol. eprint: cond-mat/9906243v1 (cond-mat.str-el).

[2] H. Y. Yang and K. P. Schmidt. "Effective models for gapped phases of strongly correlated quantum lattice models". *EPL (Europhysics Letters)* 94.1 (2011), p. 17004.

[3] Serkan Sahin, Kai Phillip Schmidt, and Román Orús. "Entanglement continuous unitary transformations". *EPL (Europhysics Letters)* 117.2 (2017), p. 20002.

[4] B. Sriram Shastry and Bill Sutherland. "Excitation Spectrum of a Dimerized Next-Neighbor Antiferromagnetic Chain". *Phys. Rev. Lett.* 47 (13 1981), pp. 964–967.

[5] Klaus Fabricius, Ute Löw, and Joachim Stolze. "Dynamic correlations of antiferromagnetic spin- XXZ chains at arbitrary temperature from complete diagonalization". *Phys. Rev. B* 55 (9 1997), pp. 5833–5846.

[6] J. Jensen et al. "Lineshape of the singlet-triplet excitations in the dimer system $Sr_3Cr_2O_8$ to first order in the high-density $1/z$ expansion". *Phys. Rev. B* 89 (13 2014), p. 134407.

[7] Benedikt Fauseweh, Joachim Stolze, and Götz S. Uhrig. "Finite temperature line-shapes of hard-core bosons in quantum magnets: A diagrammatic approach tested in one dimension". *Phys. Rev. B* 90 (Aug. 2014), p. 024428. eprint: 1402.4359v2 (cond-mat.str-el).

[8] Benedikt Fauseweh and Götz S. Uhrig. "Low temperature thermodynamics of multi-flavored hardcore bosons by the Brückner approach". *Phys. Rev. B* 92 (Dec. 2015), p. 214417. eprint: 1507.03793v2 (cond-mat.str-el).

[9] Stéphane Ty and Bertrand I. Halperin. "Damping of spin waves in a two-dimensional Heisenberg antiferromagnet at low temperatures". *Phys. Rev. B* 42 (4 1990), pp. 2096–2115.

[10] S. P. Bayrakci et al. "Lifetimes of Antiferromagnetic Magnons in Two and Three Dimensions: Experiment, Theory, and Numerics". *Phys. Rev. Lett.* 111 (1 2013), p. 017204.

[11] E. S. Klyushina et al. "Magnetic excitations in the $S = \frac{1}{2}$ antiferromagnetic-ferromagnetic chain compound $BaCu_2V_2O_8$ at zero and finite temperature". *Phys. Rev. B* 93 (24 2016), p. 241109.

[12] Ch. Rüegg et al. "Quantum Statistics of Interacting Dimer Spin Systems". *Phys. Rev. Lett.* 95 (26 2005), p. 267201.

[13] D. A. Tennant et al. "Anomalous dynamical line shapes in a quantum magnet at finite temperature". *Phys. Rev. B* 85 (1 2012), p. 014402.

[14] D. L. Quintero-Castro et al. "Asymmetric Thermal Line Shape Broadening in a Gapped 3D Antiferromagnet: Evidence for Strong Correlations at Finite Temperature". *Phys. Rev. Lett.* 109 (12 2012), p. 127206.

[15] Benedikt Fauseweh. "Dynamic Correlations in One-Dimensional Quantum Magnets at Finite Temperature". PhD thesis. Technische Universität Dortmund, 2016.

[16] R. Coldea, D. A. Tennant, and Z. Tylczynski. "Extended scattering continua characteristic of spin fractionalization in the two-dimensional frustrated quantum magnet Cs_2CuCl_4 observed by neutron scattering". *Phys. Rev. B* 68 (13 2003), p. 134424.

[17] Luca F. Tocchio et al. "One-dimensional spin liquid, collinear, and spiral phases from uncoupled chains to the triangular lattice". *Phys. Rev. B* 89 (23 2014), p. 235107.

[18] R. Coldea et al. "Experimental Realization of a 2D Fractional Quantum Spin Liquid". *Phys. Rev. Lett.* 86 (7 2001), pp. 1335–1338.

[19] R. Coldea et al. "Direct Measurement of the Spin Hamiltonian and Observation of Condensation of Magnons in the 2D Frustrated Quantum Magnet Cs_2CuCl_4". *Phys. Rev. Lett.* 88 (13 2002), p. 137203.

[20] S. A. Zvyagin et al. "Direct Determination of Exchange Parameters in Cs_2CuBr_4 and Cs_2CuCl_4: High-Field Electron-Spin-Resonance Studies". *Phys. Rev. Lett.* 112 (7 2014), p. 077206.

[21] Simon Streib. "Theoretical investigations of the spin-1/2 triangular lattice antiferromagnet Cs_2CuCl_4 in the spin-liquid and high-magnetic-field regimes". PhD thesis. Johann Wolfgang Goethe-Universität in Frankfurt am Main, 2015.

[22] S. Gerhold et al. "X-ray absorption spectroscopy of single-crystalline $(VO)_2P_2O_7$: Electronic structure and possible exchange paths". *Phys. Rev. B* 63 (7 2001), p. 073103.

[23] D. C. Johnston et al. "Magnetic susceptibility of $(VO)_2P_2O_7$: A one-dimensional spin-1/2 Heisenberg antiferromagnet with a ladder spin configuration and a singlet ground state". *Phys. Rev. B* 35 (1 1987), pp. 219–222.

[24] D. A. Tennant et al. "Excitation Spectrum and Superexchange Pathways in the Spin Dimer $VODPO_4\cdot\frac{1}{2}D_2O$". *Phys. Rev. Lett.* 78 (26 1997), pp. 4998–5001.

[25] Jun Kikuchi et al. "Coexistence of double alternating antiferromagnetic chains in (VO)_2P_2O_7 : NMR study". *Phys. Rev. B* 60 (Feb. 1999), p. 6731. eprint: `cond-mat/9902205v1` (cond-mat.str-el).

[26] P. Millet et al. "Magnetic properties of the coupled ladder system MgV_2O_5" (Feb. 1998), Phys. Rev. B. eprint: `cond-mat/9802029v1` (cond-mat.str-el).

[27] A. W. Garrett et al. "Magnetic Excitations in the $S = 1/2$ Alternating Chain Compound $(VO)_2P_2O_7$". *Phys. Rev. Lett.* 79 (4 1997), pp. 745–748.

[28] G. S. Uhrig and B. Normand. "Magnetic properties of $(VO)_2P_2O_7$ from frustrated interchain coupling". *Phys. Rev. B* 58 (22 1998), R14705–R14708.

[29] Christian Knetter and Goetz S. Uhrig. "Triplet Dispersion in CuGeO_3: Perturbative Analysis". *Phys. Rev. B* 63 (Apr. 2001), p. 94401. eprint: `cond-mat/0004243v1` (cond-mat.str-el).

[30] Franz Wegner. "Flow equations for Hamiltonians". *Advances in Solid State Physics 40*. Ed. by Bernhard Kramer. Berlin, Heidelberg: Springer Berlin Heidelberg, 2000, pp. 133–142. ISBN: 978-3-540-44560-9.

[31] G. S. Uhrig and B. Normand. "Magnetic properties of (VO)_2P_2O_7: two-plane structure and spin-phonon interactions". *Phys. Rev. B* 63 (Oct. 2001), p. 134418. eprint: `cond-mat/0010168v1` (cond-mat.str-el).

[32] Christian Knetter, Kai P Schmidt, and Götz S Uhrig. "The structure of operators in effective particle-conserving models". *Journal of Physics A: Mathematical and General* 36.29 (2003), p. 7889.

[33] E. S. Klyushina et al. "Magnetic excitations in the S = 1/2 antiferromagnetic-ferromagnetic chain compound BaCu2V2O8 at zero and finite temperature". *Phys. Rev. B* 93 (July 2016), p. 241109. eprint: `1602.06184v3` (cond-mat.str-el).

[34] Alexander L Fetter and John Dirk Walecka. *Quantum theory of many-particle systems*. Courier Corporation, 2012.

[35] V. N. Kotov et al. "Novel Approach to Description of Spin-Liquid Phases in Low-Dimensional Quantum Antiferromagnets". *Phys. Rev. Lett.* 80 (26 1998), pp. 5790–5793.

[36] Wolfgang Nolting. *Grundkurs Theoretische Physik 7*. Springer Spektrum, 2015.

[37] Gordon Baym. "Self-Consistent Approximations in Many-Body Systems". *Phys. Rev.* 127 (4 1962), pp. 1391–1401.

[38] Leonardo Dagum and Ramesh Menon. "OpenMP: An Industry-Standard API for Shared-Memory Programming". *IEEE Comput. Sci. Eng.* 5.1 (1998), pp. 46–55. ISSN: 1070-9924.

[39] Matteo Frigo and Steven G. Johnson. "The Design and Implementation of FFTW3". *Proceedings of the IEEE* 93.2 (2005). Special issue on "Program Generation, Optimization, and Platform Adaptation", pp. 216–231.

[40] Hsi-Ping Liu and Dan D. Kosloff. "Numerical evaluation of the Hilbert transform by the Fast Fourier Transform (FFT) technique". *Geophysical Journal of the Royal Astronomical Society* 67.3 (1981), pp. 791–799. ISSN: 1365-246X.

[41] Juana Moreno and José M. Soler. "Optimal meshes for integrals in real- and reciprocal-space unit cells". *Phys. Rev. B* 45 (24 1992), pp. 13891–13898.

[42] *boost.org*. `http://www.boost.org/`. Accessed: 2017-03-25.

[43] *OpenCL™ Optimization Case Study Fast Fourier Transform*. `http://developer.amd.com/resources/articles-whitepapers/opencl-optimization-case-study-fast-fourier-transform-part-ii/`. Accessed: 2017-03-25.

[44] Patrick Johnmeyer. *Unittest++*. 2016.

Eidesstattliche Versicherung

Ich versichere hiermit an Eides statt, dass ich die vorliegende Masterarbeit mit dem Titel "Diagrammatic approach to thermal fluctuations in dimension 2" selbständig und ohne unzulässige fremde Hilfe erbracht habe. Ich habe keine anderen als die angegebenen Quellen und Hilfsmittel benutzt sowie wörtliche und sinngemäße Zitate kenntlich gemacht. Die Arbeit hat in gleicher oder ähnlicher Form noch keiner Prüfungsbehörde vorgelegen.

Ort, Datum | Unterschrift

Belehrung

Wer vorsätzlich gegen eine die Täuschung über Prüfungsleistungen betreffende Regelung einer Hochschulprüfungsordnung verstößt handelt ordnungswidrig. Die Ordnungswidrigkeit kann mit einer Geldbuße von bis zu 50.000,00 € geahndet werden. Zuständige Verwaltungsbehörde für die Verfolgung und Ahndung von Ordnungswidrigkeiten ist der Kanzler/die Kanzlerin der Technischen Universität Dortmund. Im Falle eines mehrfachen oder sonstigen schwerwiegenden Täuschungsversuches kann der Prüfling zudem exmatrikuliert werden (§ 63 Abs. 5 Hochschulgesetz - HG -).

Die Abgabe einer falschen Versicherung an Eides statt wird mit Freiheitsstrafe bis zu 3 Jahren oder mit Geldstrafe bestraft.

Die Technische Universität Dortmund wird ggf. elektronische Vergleichswerkzeuge (wie z.B. die Software "turnitin") zur Überprüfung von Ordnungswidrigkeiten in Prüfungsverfahren nutzen.

Die oben stehende Belehrung habe ich zur Kenntnis genommen.

Ort, Datum | Unterschrift